Towards the fast neutron-induced isotope production of ^{99m}Tc via the ^{102}Ru$(n,\alpha)^{99}$Mo reaction

by

Melanie Gascoine

B.Sc., McMaster University, 2018

Thesis Submitted in Partial Fulfillment of the
Requirements for the Degree of
Master of Science

in the
Department of Chemistry
Faculty of Science

© Melanie Gascoine 2021
SIMON FRASER UNIVERSITY
Summer 2021

Copyright in this work is held by the author. Please ensure that any reproduction or re-use is done in accordance with the relevant national copyright legislation.

Declaration of Committee

Name:	**Melanie Gascoine**
Degree:	**Master of Science**
Thesis title:	**Towards the fast neutron-induced isotope production of ^{99m}Tc via the ^{102}Ru$(n,\alpha)^{99}$Mo reaction**
Committee:	**Chair:** Robert Britton Professor, Chemistry
	Daniel Leznoff Supervisor Professor, Chemistry
	Byron Gates Committee Member Professor, Chemistry
	Caterina Ramogida Committee Member Assistant Professor, Chemistry
	Cornelia Hoehr Examiner Adjunct Professor, Physics TRIUMF

Abstract

Radioactive isotopes are widely used in medicine for diagnostic and therapeutic procedures. The most commonly used isotope is technetium-99m (^{99m}Tc), a product of β-decay of a molybdenum-99 (^{99}Mo) nucleus, which is currently commercially produced using nuclear reactors. An alternative method of medical grade radioisotope production is required to sustain the demand as nuclear reactors are decommissioned. The proposed method of isotope production which will be discussed in this thesis is to use fast neutrons ($\sim$14.1 MeV) to induce an $^{102}\mathrm{Ru}(n,\alpha)^{99}\mathrm{Mo}$ reaction. The Nuclear Science Laboratory (NSL) at Simon Fraser University (SFU) has a Deuterium-Tritium (D-T) Thermo Fisher P385 Neutron Generator (NG) which will be used for the neutron production, as well as 'state of the art' gamma ray spectrometers that will be used for experimental analysis. A series of experiments are discussed in this thesis to prove the viability of fast neutron induced isotope production.

Keywords: Neutron activation analysis; Gamma-ray spectroscopy; Neutron induced isotope production; Medical isotopes

Table of Contents

List of Tables

List of Figures

List of Symbols and Abbreviations

abs.	Absolute
arb.	Arbitrary
CAMAC	Computer Automated Measurement And Control
D-T	Deuterium-Tritium
d.o.f	Degrees Of Freedom
DAQ	Data Acquisition
eV	Electron volt ($\sim 1.602 \times 10^{-19}$ J in SI base units)
Geant4	Geometry and Tracking version 4
GEARS	Germanium detector for Elemental Analaysis and Radioactivity Studies
HPGe	High Purity Germanium
Hz	Hertz (1 s^{-1} in SI base units)
int.	Interest
irr.	Irradiation
keV	Kiloelectron volt (10^3 eV)
kHz	Kilohertz (10^3 Hz)
LN2	Liquid Nitrogen
MeV	Megaelectron volt (10^6 eV)
MHz	Megahertz (10^6 Hz)
MIDAS	Maximum Integrated Data Acquisition System
NG	Neutron Generator

NIM	Nuclear Instrument Module
NSL	Nuclear Science Laboratory
ODE	Ordinary Differential Equation
p.i.	post irradiation
ref.	Reference
rel.	Relative
SFU	Simon Fraser University

There are a large number of symbols used in the equations defined in this thesis. Many of the symbols are context-dependent, or dependent on other equations or symbols, and thus a complete list of symbols will not be provided. Alternatively, each symbol will be defined in the text where they occur. Symbols have been assigned according to the following criteria:

1. Standard notation is used
2. Symbols should not be multiply defined whenever possible.

If there is a conflict, the criteria is followed in order, with the addition of a subscript to differentiate between the definitions. Unless otherwise stated, uncertainties are quoted at the 1 σ level, and given in parenthesis to match the last given decimal place. For example, 10.92(6) corresponds to 10.92 ± 0.06.

Chapter 1

Introduction

The most commonly used radioisotope in medical diagnostic procedures is technetium-99m (^{99m}Tc), which is a long lived excited state of ^{99}Tc, and a product of the beta (β) decay of a molybdenum-99 (^{99}Mo) nucleus. The current commercially viable method of production occurs within nuclear reactors in which uranium targets are bombarded by thermal neutrons ($\sim$0.025 eV) resulting in fission of the uranium nuclei to produce small amounts of ^{99}Mo. As nuclear reactors are decommissioned, an alternative method is required to sustain the demand for medical grade radioisotopes, which are isotopically pure and have a high specific activity.

The proposed method of isotope production that will be discussed in this thesis is through the use of fast neutrons (14.1 MeV) produced using the Deuterium-Tritium (D-T) Neutron Generator (NG) housed at the Nuclear Science Laboratory (NSL) at Simon Fraser University (SFU). Natural ruthenium is irradiated with fast neutrons to remove an alpha (α) particle from the ruthenium nuclei and produce ^{99}Mo. The advantage of this production method is that the separation of the product from the target begins during the irradiation; upon the absorption of the neutron or the emission of the alpha particle, a nuclear recoil will occur imparting enough energy on the nucleus to overcome intermolecular forces, allowing the product to recoil out of the target. Following the separation by recoil, the target can be designed such that the product recoils into a solution that can be easily separated from the natural ruthenium through chemical separation methods to obtain a medical grade product. In order to pursue neutron activation for isotope production, a series of preliminary experiments were completed to determine the amount of an isotope that could realistically be produced using the NG, and the quality of the product that can be achieved.

This thesis will begin with background theory for understanding gamma-ray (γ-ray) decay and the types of detectors used at the NSL in Chapter 2. γ-ray spectroscopy is the detection method of choice and is used for the analysis of all radioactive samples. The current spectrometer being used at the NSL is the Germanium Detector for Elemental Analysis and Radioactivity Studies (GEARS), a passively shielded, High-Purity Germanium (HPGe)

detector. GEARS has been set up for high energy resolution and time resolved γ-ray spectroscopy, and has been successfully used for the identification and quantification of radioisotopes within samples. Chapter 3 consists of a description of GEARS including the physical set-up and data acquisition (DAQ) specifications, followed by the detector characterization and spectrum analysis procedure used for this thesis. Chapter 4 will introduce the isotope producer project. A brief history and motivation for the production of medical isotopes is followed by a detailed overview of the NSL NG facilities, a dicussion about neutron interactions, and the Szilard-Chalmers reaction. The experimental set up for the isotope production is discussed in Chapter 5, detailing the proposed device and analytical methods that will be used in the planning stage for testing the set-up. Experiments completed for the irradiation set-up and preliminary separation are completed, with the analysis of results shown in Chapter 6. This thesis concludes with Chapter 7, which includes a discussion about future experiments that will be undertaken for the development of the isotope production device.

Chapter 2

Principles of γ-ray spectroscopy

2.1 Principles of γ-ray decay

γ-ray decay can occur following α- or β- decay, or as the result of direct population of excited states that decay via gamma emission [1]. In numerous cases, α- and β-decay populate excited states of the daughter nuclei, which decay to the ground state through the emission of one or more gamma-rays. γ-ray decay typically occurs on the order of nanoseconds (ns); however, lifetimes between 10^{-15} to 10^{15} s can occur [2]. γ-rays have energies in the range of 0.1 to 10 MeV and, following conservation of energy, are approximately equal to the energy difference between the transitioning nuclear states. The discrepancy between the γ-ray energy and the energy difference between the tranisitioning nuclear states is due to the recoil of the nucleus upon decay. Gamma emitters have a unique collection of characteristic γ-rays that can be detected to differentiate between isotopes within a sample.

As an example, the decay scheme of a commonly used laboratory isotope, cobalt-60 (^{60}Co), is shown in Fig. 2.1. ^{60}Co first undergoes β-decay to an excited state of nickel-60 (^{60}Ni*, where * denotes an excited state) before relaxing to the ground state of ^{60}Ni by emitting γ-rays. Characteristic γ-rays are 1173.2 and 1332.5 keV, which are emitted in a cascade with an intensity, or probability of 99.85% and 99.98%, respectively. Other γ-rays can occur as seen in Fig. 2.1; however, at a much lower intensity that is typically not visible on a γ-ray spectrum. For ^{60}Co, 100% of the radioactive nuclei will decay via β-decay and subsequently emit γ-rays. By observing the intensity of characteristic γ-rays, the strength and, thus, the activity of the source can be determined [3].

The intensity or number of γ-rays emitted is related to the number of radioactive nuclei in the sample or source following

$$N(t) = br(E_\gamma) N_0 e^{-\lambda t}, \tag{2.1}$$

where *N(t)* is the number of radioactive nuclei emitted as a function of time, $br(E_\gamma)$ is the branching ratio of the γ-ray with energy E_γ, λ is the decay constant, and N_0 is the number of radioactive nuclei in the source under observation at $t = 0$ [2]. The decay constant is

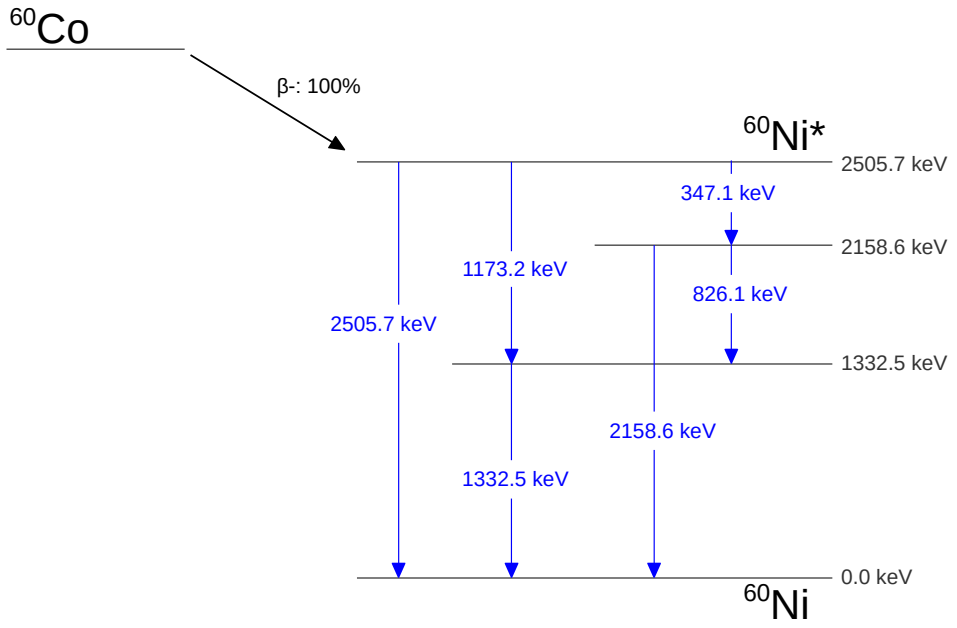

Figure 2.1: A decay scheme of ^{60}Co. Following β^- decay to ^{60}Ni*, with a half life of 1925.28 days, the excited state transitions to ground via γ-ray emissions, which are shown in blue, with the most probable decay path being a cascade. The first γ-ray in the cascade has an energy of 1173 keV with an intensity of 99.85%, and the second has an energy of 1332 keV with an intensity of 99.98%. The intensity of the decay is relative to the total number of decaying ^{60}Co nuclei.

related to the half life, $t_{1/2}$, which is characteristic of each individual isotope and defines the amount of time it takes for half of the total amount of radioactive nuclei in the source to decay. The lifetime, τ, of the nucleus is also related to the decay constant and $t_{1/2}$ following

$$\lambda = \frac{\ln(2)}{t_{1/2}} = \frac{1}{\tau}. \tag{2.2}$$

Finally, the activity, A, is given in units of Becquerels (Bq) or decays per second and is related to the number of emitted γ-rays following

$$A(t) = \lambda N(t). \tag{2.3}$$

2.2 γ-ray interactions with matter

There are three major ways that γ-rays interact with matter; photoelectric absorption, Compton scattering, and pair production [4]. All interaction mechanisms result in the partial or complete absorption of energy, and when measured using γ-ray spectroscopy, result in characteristic peaks as shown in Fig. 2.2.

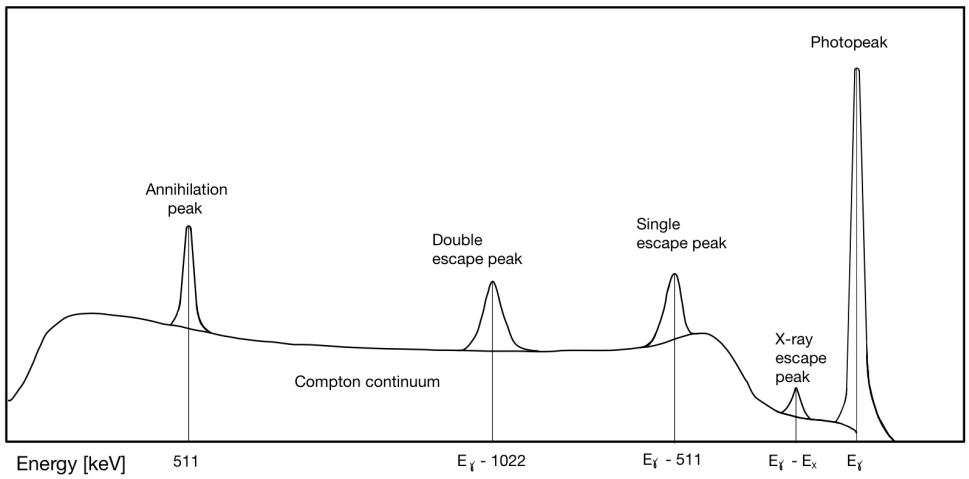

Figure 2.2: An illustration of a γ-ray spectrum of a monoenergetic source with $E_\gamma > 1.022$ MeV. The features and peaks shown in this spectrum are a result of the incident photon interacting with the detection medium through photoelectric absorption, compton scattering, or pair production. See Sec. 2.2 for details. [3].

Photoelectric Absorption

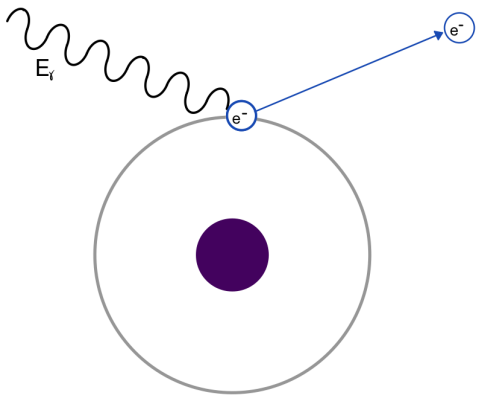

Figure 2.3: A diagram of the photoelelectric absorption process, in which an incoming γ-ray with energy E_γ, deposits its full energy onto an electron within the absorbing material. The electron is then liberated from its atomic shell, with energy given by Eq. 2.4.

During photoelectric absorption, the photon interacting with an atom in the detector medium deposits all of its energy, resulting in the ejection of a photoelectron from one of the atoms' bound shells [3]. A schematic of this process is seen in Fig. 2.3. The ejected electron energy (E_{e^-}) given by

$$E_{e^-} = E_\gamma - E_b \tag{2.4}$$

where E_γ is the energy of the incident photon, and E_b is the binding energy of the photoelectron in its original shell. The vacancy left behind by the ejected electron is filled quickly by rearrangement of electrons, which will result in the emission of a characteristic X-ray, or Auger electron. If the X-ray escapes the detector medium, a characteristic X-ray escape peak can be seen at $E = E_\gamma$ - $E_{\text{X-ray}}$, as seen in the illustration of the spectrum in Fig. 2.2. For photons with large energies where $E_b \ll E_\gamma$, the energy of the emitted electron can be approximated as $E_{e^-} \approx E_\gamma$. Photoelectric absorption is the dominating mode of interaction for low energy γ-rays, and absorbing materials with high atomic number [3].

Compton Scattering

During a Compton scattering process the incident γ-ray scatters off of the absorbing electron, transferring partial energy to the electron that is then ejected as a recoil electron. The scattered γ-ray is emitted at an angle θ while the recoiling electron is emitted with an angle ϕ, both with respect to the incident photon. A schematic of the Compton scattering process is shown in Fig. 2.4.

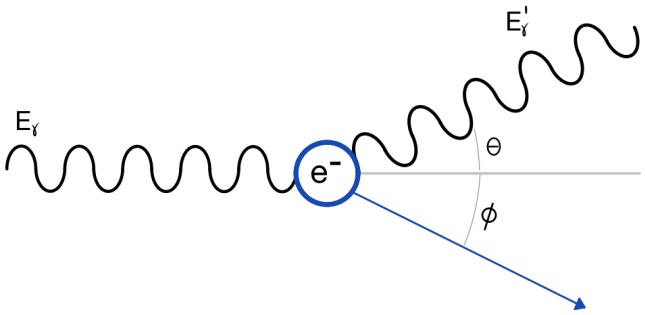

Figure 2.4: A diagram of the Compton scattering process in which the incident γ-ray collides with an electron, scattering at an angle θ with respect to its original trajectory. The electron recoils at an angle ϕ with respect to the original γ-ray trajectory.

The energy of the scattering photon, E'_γ, can be determined by conservation of energy and momentum of the system, which results in

$$E'_\gamma = \frac{E_\gamma}{1 + \frac{E_{\gamma_i}}{m_0 c^2}(1 - \cos\theta)}, \tag{2.5}$$

and the recoil electron has energy given by

$$E_{e^-} = E_\gamma - E'_\gamma. \tag{2.6}$$

Due to the dependence of electron energy on the scattering angle, θ, Compton scattering results in a continuum of energies in the γ-ray spectrum called the Compton continuum.

For γ-rays of high energy, the resulting Compton continuum can result in high background, concealing the presence of low energy γ-rays in a spectrum [3]. Compton scattering is the dominant mode of interaction for mid-range γ-ray energies between a few hundred keV and 5 MeV. In the case where the scattered γ-ray interacts again with the detector via the photoelectric effect, with no loss of electrons from the detection medium, this event will contribute to the full-energy photopeak observed within the spectrum. A spectrum with characteristic features of Compton scattering is shown in Fig. 2.2.

Pair Production

Pair production can occur if the energy of the incident γ-ray exceeds 1.022 MeV, or two times the rest mass energy of an electron. This interaction occurs within the Coulomb field of the atoms in the absorbing medium and produces an electron/positron pair, with combined energy of 1.022 MeV. If the γ-ray has more energy than 1.022 MeV, the remaining energy is distributed between the electron and positron as kinetic energy. The kinetic energies of the electron and positron is therefore given by

$$E_{e^+} + E_{e^-} = E_\gamma - 2m_0c^2, \tag{2.7}$$

where m_0 is rest mass. Both the electron and positron will lose energy by interacting with the absorbing medium, with the positron eventually interacting with a local electron, annihilating, and producing two annihilation photons each with 0.511 MeV energy emitted at $\sim$180° with respect to one another. A schematic showing the pair production process is shown in Fig. 2.5.

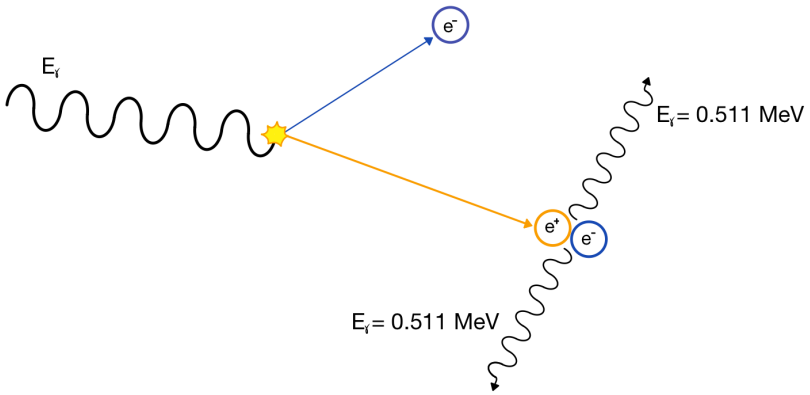

Figure 2.5: A diagram of the pair production process in which the incident γ-ray interacts with the electric field of a nucleus in the absorbing medium, to create an electron/positron pair. The positron interacts with an atomic electron and annihilates, creating 2 annihilation photons emitted at an angle of 180° with respect to one another, both with E = 0.511 MeV.

Pair production can result in two distinct peaks in a spectrum at 0.511 MeV and 1.022 MeV less than the energy of the original γ-ray. These two peaks are called a single escape peak and a double escape peak, respectively, as they occur when either one or both of the annihilation photons escapes the detection medium [3]. Pair production is the dominant mode of interaction for high energy γ-rays between 5 - 10 MeV. The single escape peak and double escape peak that result from pair production are depicted in the spectrum shown in Fig. 2.2.

2.3 γ-ray detection systems

A standard technique in nuclear spectroscopy is the study of γ-rays; they are easily detected as they experience low absorption and scattering through air. The γ-ray detector that will be discussed is the HPGe detector, known for having superior energy resolution compared to a scintillator, another commonly used γ-ray detector. Using a semiconductor detector for γ-ray spectroscopy provides a considerable number of advantages over other common alternatives, such as a scintillator or a gas counter. A semiconductor provides a linear response of pulse height vs. particle energy over a wide energy range. It also enables a high energy resolution, variable geometric configuration to match the requirements of the application, a fast pulse rise time, and an insensitivity to magnetic fields. [5]. A notable weakness of semiconductor detectors is their low efficiency, which can be compensated for by measuring strong sources, using the detectors high energy resolution, and implementing radiation protection methods that will be discussed in Sec. 3.1.1.

2.3.1 Semiconductor diode detectors

Semiconductor materials have a crystalline structure, in which the allowed atomic energy states are widened into bands that are separated by forbidden energy gaps. A simplified image of the energy bands in a semiconductor is shown in Fig. 2.6, including the valence band full of electrons, and the conduction band, which is empty and $\sim$5 eV above the valence band. For reference, the band gap of an insulator is $>$ 5 eV [5]. To promote electrons from the valence band to the conduction band, an energy greater than that of the band gap needs to be applied to the system. The energy of the band gap can be overcome through either an increase in temperature to increase thermal fluctuations, the absorption of incident radiation, or collision with an energetic charged particle. For a Ge detector, the band gap is $\sim$0.67 eV, and an energy larger than 2.96 eV is required to promote the electrons to the conduction band [3]. This discrepancy between the band gap and the required energy is due to the binding energy of the electrons that needs to be overcome in order to free the electrons from the atom.

In the case of γ-ray spectroscopy, when the incident γ-rays move through the detection medium, electrons along the γ-rays trajectory that are impacted by the radiation are

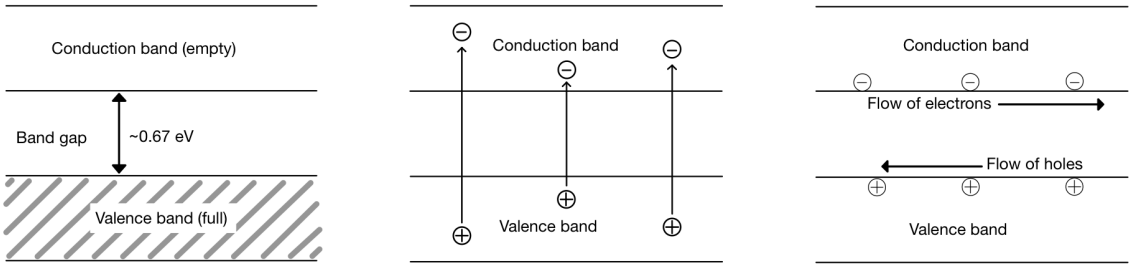

Figure 2.6: (Left) Typical band gap in a semiconductor with energy ∼0.67 eV. (Center) Excitation of electrons from the valance band to the conduction band, leaving behind holes. (Right) Accumulation of electrons in lower level of conduction band and holes in upper level of valence band. Application of an electric field results in net flow of electrons and holes in opposite directions.

promoted to the conduction band. When an electron is removed from either the valence band or lower lying energy states, a hole is left in its place creating an electron-hole pair, analogous to an ion pair in gas. Electron-hole pairs are formed within a few ps along the track of the incident radiation as a result of direct interactions, in which the γ-ray produces the electron-hole pairs, or indirect interactions, in which the γ-ray produces high energy electrons which subsequently interact with the detection medium to produce electron-hole pairs. The number of pairs produced is related to the energy of the interacting particle, and the ionization energy of the detection medium. In the case of a HPGe detector, the ionization energy is ∼2.96 eV, and an incoming γ-ray from a ^{60}Co source with $E_\gamma = 1332$ keV will result in ∼450, 000 electron-hole pairs. The small band gap is ideal for improving the energy resolution of the detector, but it allows for the thermal excitation of electrons. At any non-zero temperature, T, it is possible for themal excitation to occur in which valence electrons can gain sufficient thermal energy to cross the band gap to the conduction band. In order to prevent current resulting from thermally induced charge carriers, semiconductor detectors need to be cooled to LN2 temperatures (∼77 K).

Once they are created, the electrons and holes de-excite and congregate on either side of the band gap, as shown in the right-most panel of Fig. 2.6. Finally, in the presence of an electric field, there is net migration of the electrons and holes in opposite directions, with the holes acting like point positive charges, as shown in Fig. 2.6. The motion is due to thermal and drift velocity, where the drift velocity is a result of the applied electric field. Solid-state detectors are typically operated with an applied electric field that results in a saturated drift velocity on the order of 10^7 cm/s. Migration occurs until the electrons and holes recombine, or they are collected by an electrode with both the electrons and holes contributing to the total observed current. The time required to collect charge carriers over 0.1 cm is under 10 ns, making solid-state detectors among the fastest-responding radiation detectors [3].

2.3.2 p-n junction

Impurities in semiconductor detectors result in excess holes, or electrons within the valence band [3]. By purposefully adding small amounts of impurities on the order of 1 part per million or less via a process called doping, conductivity of a semiconductor can be increased. Doping can be done to increase the amount of either electrons or holes by replacing a small number of the crystal atoms with atoms that have either more or fewer valence electrons than the atoms in the host matrix. The resulting crystal is considered to be n-type or p-type if there are excess electrons or holes, respectively. In an n-type detector, the excess electrons are loosely bound and are promoted to the conduction band leaving behind a fixed, immobile positive charge that should not be confused with holes. In a p-type detector, there are excess vacancies in the valence bands of the detector atoms. Migrating electrons will be bound to the vacant sites to produce fixed negative charges. In n- and p-type detectors, there is an excess of holes or electrons in the valence or conduction band, increasing electrical conductivity. Semiconductor diodes take advantage of both p-type and n-type detectors by forming a p-n junction between the two types on the level of interatomic spacing. This is typically done during crystal growth to form a single crystal with different impurities from one side of the junction to the other. For HPGe detectors, the crystal volume is typically either p- or n-type, and a thin n- or p-type contact is diffused or evaporated onto the surface [3].

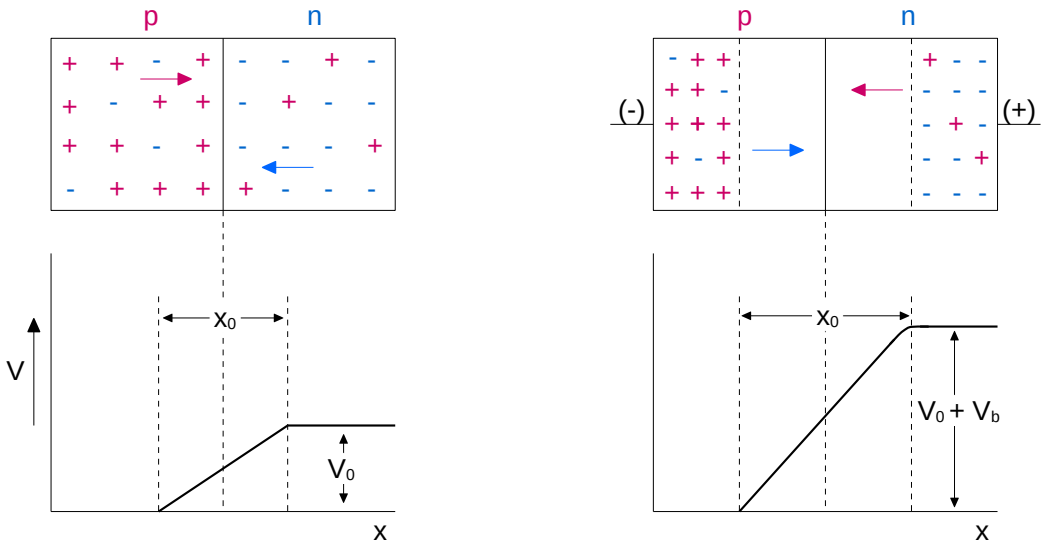

Figure 2.7: (Left) p-n junction of in a semiconductor without external voltage applied. (Right) p-n junction of a semiconductor with reverse voltage applied. The bottom two graphs shows the potential difference (V_0) between the two regions. When an external voltage (V_b) is applied with the positive pole connected to the n-side, both the potential and the depth across which the electric field exists within the two regions is increased.

At the p-n junction, there is a large population of electrons on the side of the n-type semiconductor and a large population of holes on the side of the p-type semiconductor, creating a sharp gradient. The electrons will begin to diffuse across the gap and combine with holes from the p-type material, with each electron leaving a fixed immobile positive charge. A symmetric argument is made for the holes to diffuse across the junction and combine with electrons from the n-type material, leaving behind fixed immobile negative charges. The result is a build up of a net negative charge on the p side, and a net positive charge on the n side of the junction, creating an electric field that slows and eventually stops diffusion at equilibrium.

The region of charge imbalance is called the depletion region, which extends into both p- and n-type materials. Depending on the doping levels of the p- and n-type materials, the depletion region will extend further into the material with lower doping. When a depletion region is present, a reverse bias is applied to the detector. This means the n-type contact receives a positive voltage with respect to the p-type, enhancing the natural potential difference across the junction and increasing the depletion region as shown in Fig. 2.7. By increasing the potential difference and the depletion region, recombination and loss of charge carriers is minimized. The use of p-n junctions is especially advantageous for γ-ray detectors, as the increased depletion region and high voltage increases the efficiency of the detector and ensures the charge carriers are collected before recombination.

Chapter 3

γ-ray spectroscopy at SFU

3.1 The GEARS detector

The current detection system used in the NSL at SFU is the GEARS detector. GEARS is a GEM Series p-type Coaxial High Purity Germanium Radiation Detector, designed to detect γ-rays in the energy range of $\sim$0.04 MeV to 10 MeV. ORTEC GEM series detectors are a line of P-type coaxial HPGe detectors designed for the typical γ-ray energy range of 40 keV and upwards [6].

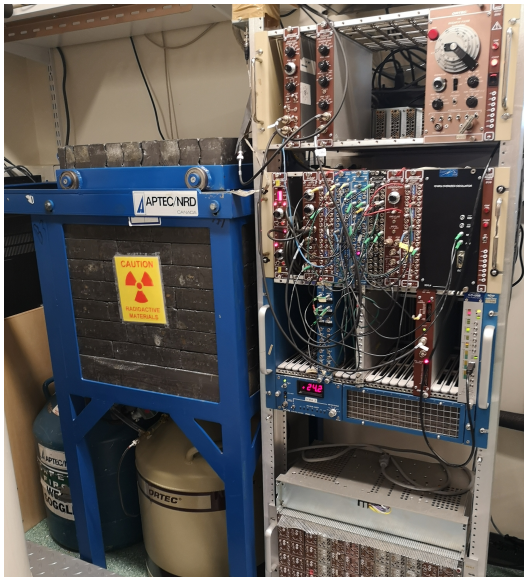

Figure 3.1: (Left) The interior of the shielding of the GEARS detector is shown, with a Cd/Cu cylinder surrounding an Al can, which encases the detection crystal. [7]. (Right) The lead shielding around the GEARS detector is pictured next to the DAQ system.

The HPGe crystal is housed in a cryostat and held under vacuum within a 1.27 mm thick aluminum (Al) can, surrounded by a copper (Cu)/cadmium (Cd) cylinder. The outer shielding is a lead box with dimensions 50 cm $\times$ 50 cm $\times$ 64 cm. The interior and exterior of the GEARS detector is shown in Fig. 3.1. GEARS uses passive shielding to minimize background radiation, which is a method to protect against radiation from the source. This method is implemented by placing material between the source of radiation and radiosensi-

tive material to absorb this radiation before it reaches the detector. In the case of GEARS, the shield is made up of multiple layers of absorbing materials; a low activity lead housing, Cu/Cd cylinder, and finally the Al can. The reason multiple layers are used is because ionizing radiation interacting with the shielding can result in the emission of low energy X-rays and electrons, as described in Sec. 2.2. By having layers of shielding made of consecutively smaller atoms, the X-rays and electrons ejected from the shielding material will also have decreased energy, eventually resulting in X-rays below the DAQ energy threshold cut off. With three layers of shielding, the amount of background interacting with the HPGe detector is decreased by a factor of ∼100 [8]. The DAQ energy threshold cut off will further decrease the amount of background detected by removing any low energy radiation seen by the detector crystal.

It is important to note that passive shielding is only effective at reducing the background from external sources. This means that any background produced by the source itself will be detected and, providing the energy is above the low energy threshold, will be reflected on the spectrum.

The GEARS DAQ system carries out energy and timing signal processing to accurately measure the energy of the detected γ-ray, as well as the time at which it is detected. Timing measurements are enabled by a 10 MHz oven-controlled crystal oscillator acting as the clock, which registers a time stamp at 100 ns intervals. When processing the energy signal, a low and high energy threshold are set to exclude background energies and overamplified signals. Ideally, the lower threshold is set as low as possible using the 59.54 keV γ-ray characteristic to 241-Americium (^{241}Am) being used as a benchmark, while the upper threshold is restricted by the limits of the electronics being used for the signal processing. For GEARS, the upper threshold is set to ∼3700 keV. Further specifications concerning the DAQ are discussed in the Sec. 3.1.1.

The GEARS detector operates at liquid nitrogen (LN2) temperatures ($<$ 100 K). A 50 L LN2 dewar refilled twice a week provides cooling via a Cu cold finger which thermally connects the crystal to the dewar. The GEARS LN2 filling procedure can be found at the NSL website [9].

3.1.1 GEARS DAQ

To process the signals coming from the detector, Computer Automated Measurement and Control (CAMAC) and Nuclear Instrument Module (NIM) modules are employed [10]. When ionizing radiation interacts with the detection medium, the electron-hole pairs are collected to generate a current and produce a signal which is split to produce a fast timing pulse and a slow energy pulse. The fast timing pulse is derived in order to provide accurate timing information, optimize the length of time required to detect a single pulse, and prevent other signals from being processed at the same time. The slow energy pulse is derived in order to have an accurate energy measurement. A full description of the signal processing

and the specific modules used can be found at Ref. [7]. Data is collected using a Maximum Integrated Data Acquisition System (MIDAS) systems control software. The saved data is in the MIDAS binary file format, and contains all energy and timing information from the measurement, organized into event structures. The data can then be sorted and extracted using a set of in-house C programs depending on the needs of the user. To analyse spectra, the C programs write the data to a modified version of the RadWare spectrum format (.spx) that can be analysed by the RadWare gf3 software, as discussed in Sec. 3.1.2. The C programs are referred to as GEARSsort and are derived from TIPsort codes that can be locate

3.1.2

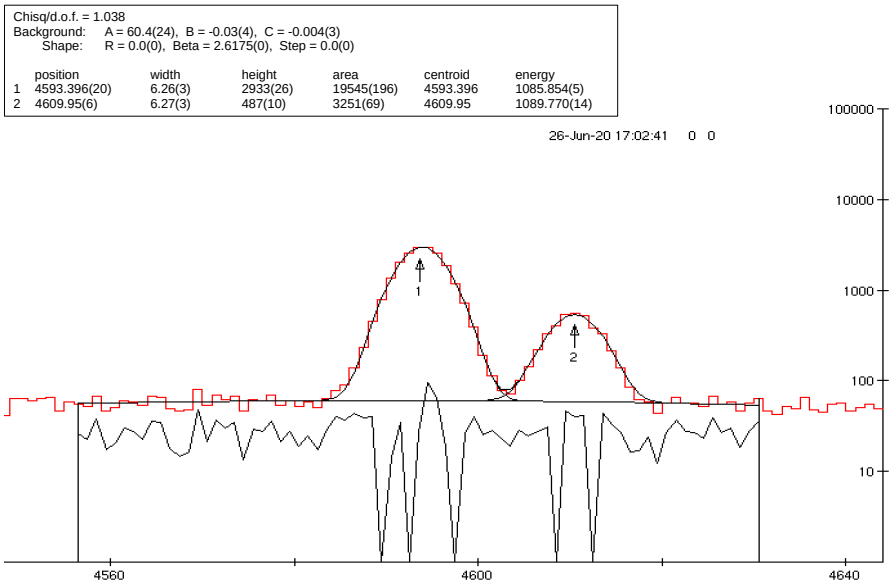

Figure 3.2: An example of two peaks fit using RadWare gf3 software. Information reported (from left to right of the results box) is centroid position, full width at half maximum, height of peak, area under the peak, the centroid position, and the corresponding energy which depends on the calibration. The black curve shows the baseline for the background.

Once a spectrum file has been created, it can be analyzed using RadWare, a software package used for interactive graphical analysis of γ-ray spectra. Specfically the gf3 program, designed for general spectrum manipulation, fitting, and analysis of one-dimensional spectra, is used [12]. The gf3 program can fit a portion of a spectrum summing up to 15 peaks on a quadratic background. Peak fitting is done using the least-squares method of analysis, with each peak fit to either a gaussian or skewed gaussian, with or without a step function in order to correct for the Compton background on the low energy side of the peak. The information reported from a peak fit is centroid position, peak area, peak width, peak height, and centroid energy, in which the accuracy depends on whether or not the energy

calibration was completed. An example of a peak fit using gf3, along with the reported information is shown in Fig. 3.2. Spectrum plotting is done using the RadWare plotting software [13].

3.2 Characterization of GEARS

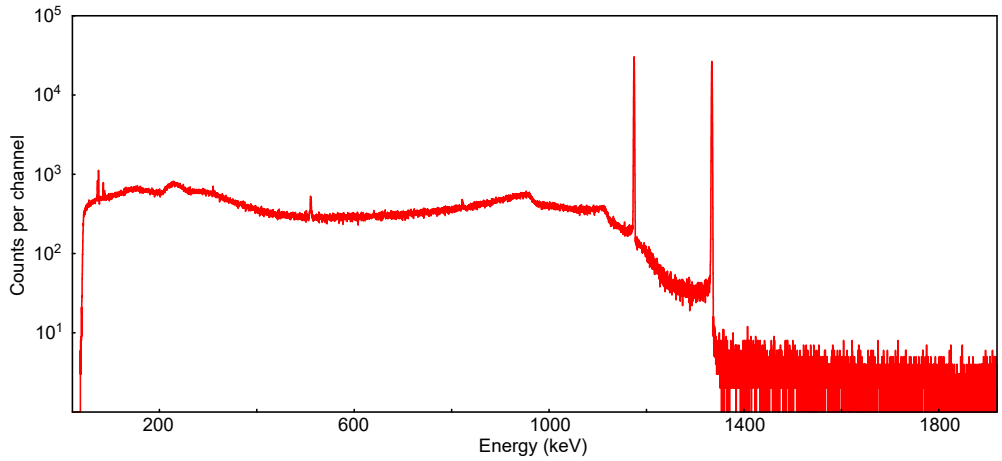

Figure 3.3: ^{60}Co spectrum taken with GEARS. The source was positioned 10.5 cm above the can.

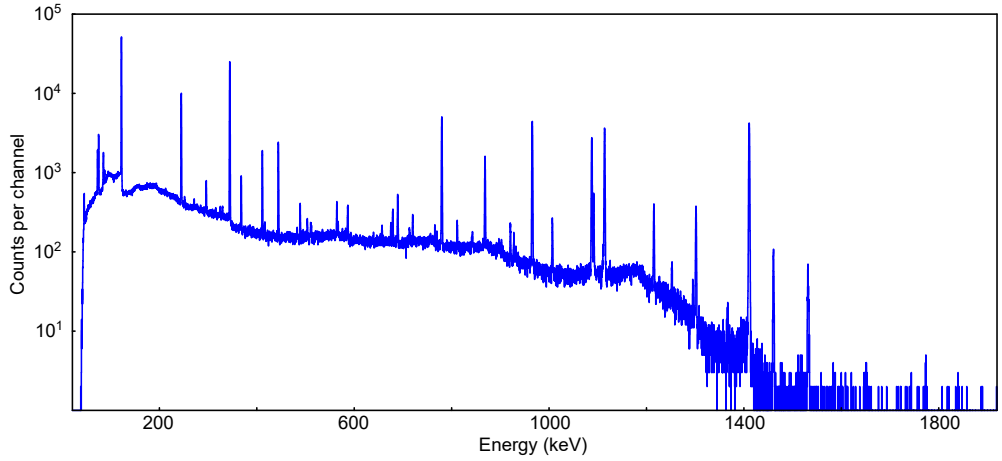

Figure 3.4: ^{152}Eu spectrum taken with GEARS. The source was positioned 10.5 cm above the can.

Before taking a measurement, GEARS needed to be characterized, or rather GEARS response to ionizing radiation, specifically γ-rays, needed to be determined. GEARS is regularly shut down during long periods of inactivity, thus allowing for potential impurities to be introduced into the crystal when it is cooled to LN2 temperatures, as previously discussed in Chapter 2. Therefore, prior to taking sample measurements GEARS should be

charaterized in order to establish the energy and efficiency response of the detector for the γ-ray energies of interest. Characterization of GEARS completed for measurements taken in this thesis will be shown in the following sections. The γ-ray spectra used for energy and efficiency calibrations are shown in Fig. 3.3 and Fig. 3.4. ^{60}Co is a commonly used isotope for calibration due to its two distinct γ-rays at 1173 keV and 1332 keV, with well known branching ratios as shown in Fig. 2.1. In order to calibrate over a wide range of energies, europium-152 (^{152}Eu) is used as it emits many γ-rays over a wide energy range with well known branching ratios.

Energy calibration

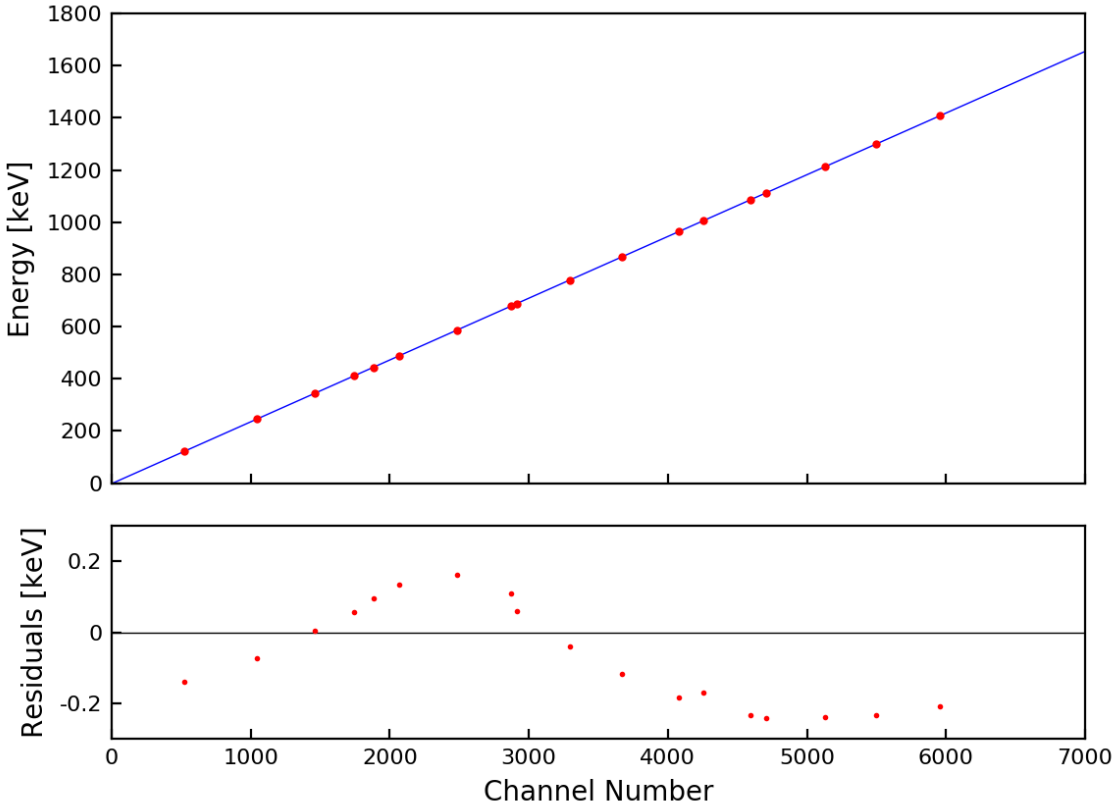

Figure 3.5: Energy calibration of GEARS completed using ^{152}Eu source. Residuals show a non-linear trend, but this does not affect the analysis of data in this thesis.

The first step to characterize the detector is to establish the energy-channel calibration. Different isotopes in a sample can be distinguished from one another due to each γ-decaying isotope having its own characteristic energy spectrum, as seen in Fig. 3.3 and 3.4. An energy-channel calibration is crucial in order to accurately identify the energy of the detected γ-rays. For this thesis, all GEARS measurements were taken in the same cooling period, and a single energy calibration has been completed using the least squares formalism defined in

Appendix B [14]. For the specific case of the energy-channel calibration, the fitting function used is

$$E_\gamma(\varsigma) = a_0 + a_1\varsigma + a_2\varsigma^2, \tag{3.1}$$

where E_γ is the energy of the γ-ray, and ς is the corresponding channel that the energy is mapped to by the DAQ system. The energy calibration determined using ^{60}Co and ^{152}Eu calibration sources, along with the residuals from the best fit function is shown in Fig. 3.5. The energy spectrum was calibrated for energies between the 244.6974 keV and 1408.013 keV. This range encompasses the relevant γ-ray energies evaluated in this thesis.

Efficiency calibration

Following the energy calibration, the efficiency of the detector can be characterized. The efficiency relates the number of detected events to the number of γ-rays that were actually emitted from the source and is determined using a source with a well known activity and branching ratios, and only interactions in which the full energy of the incident γ-ray was deposited. The relationship between the efficiency and the number of γ-rays observed in a photopeak of energy E_γ, $N(E_\gamma)$, is given by

$$\epsilon(E_\gamma) = \frac{N(E_\gamma)}{A(t) \cdot br(E_\gamma) \cdot t_{live}}, \tag{3.2}$$

where $A(t)$ is the activity of the source at time of the measurement, $br(E_\gamma)$ is the branching ratio of the γ-ray, and t_{live} is the live time of the measurement. This equation is only valid when observing isotopes in which the activity does not change by an appreciable amount during the measurement, that is to say $t_{live} \ll \tau$.

To complete an efficiency calibration, first the relative efficiency is determined, which establishes the efficiency of detecting a γ-ray with energy E_{γ_i} with respect to a reference γ-ray with energy $E_{\gamma_{ref.}}$ The chosen reference should have energy on the order of MeV to eliminate interference from electronics and signal processing, such as threshold settings. The efficiency of a detector is energy dependent, so it is also important to use a source that spans a wide range of photopeak energies. The relative efficiency calibration for GEARS was performed using a ^{152}Eu source, with a reference γ-ray energy of 1408.011 keV [15]. The relative efficiency calculation is given by

$$\frac{N_i(E_{\gamma_i})}{N_{\text{ref.}}(E_{\gamma_{\text{ref.}}})} = \frac{\epsilon_i(E_{\gamma_i})}{\epsilon_{\text{ref.}}(E_{\gamma_{\text{ref.}}})} \cdot \frac{br(E_{\gamma_i})}{br(E_{\gamma_{\text{ref.}}})} = \epsilon_{\text{rel.}} \cdot \frac{br(E_{\gamma_i})}{br(E_{\gamma_{\text{ref.}}})} \tag{3.3}$$

The ^{152}Eu spectrum taken for the efficiency calibration is shown in Fig. 3.4, with the source positioned 10.5 cm above the detector can. Photopeak counts, γ-ray energies, and corresponding relative efficiencies are shown in Table 3.1. A relative efficiency curve is established for $E_\gamma \geq 244.697$ keV, using Eq. 3.4.

Table 3.1: Relative efficiency data from a ^{152}Eu source measured with GEARS. The reference γ-ray was chosen to be 1408.013 keV, with counts scaled to 100. Scaled relative intensity is calculated according to Eq. 3.3, which relies on the relative branching ratios of the γ-ray to the reference. Errors were calculated following standard propogation of error [16].

Energy [keV]	Counts	Scaled Relative Intensity	$\epsilon_{\text{rel.}}$[arb.]
244.6974	39574(291)	36.2(2)	1094(11)
344.2785	109808(457)	127(1)	862(8)
411.1165	7930(139)	10.72(8)	740(14)
443.9606	10714(157)	13.55(9)	791(13)
488.6792	1227(75)	1.98(2)	619(38)
586.2648	1230(77)	2.18(2)	564(36)
678.623	1265(73)	2.27(2)	558(33)
688.67	2221(91)	4.10(3)	541(23)
778.9045	29490(244)	62.0(5)	476(5)
867.38	8944(145)	20.27(9)	441(7)
964.057	28774(238)	69.5(4)	414(4)
1005.27	1289(64)	3.16(5)	408(21)
1085.837	18833(190)	48.4(3)	389(5)
1112.076	24299(219)	65.5(5)	371(4)
1212.948	2403(77)	6.78(5)	354(12)
1299.142	2496(72)	7.82(6)	319(10)
1408.013	31934(239)	100.0(4)	319(3)

$$ln(\epsilon_{rel.}) = k_1 ln(E_\gamma) + k_0. \tag{3.4}$$

For the purposes of this thesis, the lower energy range $E_\gamma \leq 244$ keV can be neglected without impacting the data analysis. The parameters k and b are found using the method of least squares, as detailed in Appendix A, and shown in Table 3.2.

Table 3.2: Parameters for efficiency calibration determined by fitting ^{152}Eu data from Table 3.1 to Eq. 3.4 using the Least Squares method in Appendix A. Errors are given for 1σ confidence interval.

Parameter	Value
k_1	-0.712(9)
k_0	10.92(6)

Once a relative efficiency curve has been established, the data is then scaled using an activity calibrated source in order to determine the absolute efficiency, defined as

$$\epsilon_{abs.} = \frac{\text{number of recorded events}}{\text{number of } \gamma\text{-rays emitted by the source}}. \tag{3.5}$$

Absolute efficiency is determined by calibrating to sources with very low errors on their activity and no error in branching ratios. Eq. 3.2 can be rewritten as

$$\epsilon_{abs.}(E_\gamma) = \frac{N(E_\gamma)}{A(t_0)e^{\frac{t-t_0}{\tau}} \times t_{live} \times br(E_\gamma)}. \tag{3.6}$$

The source used for determining absolute efficiency is ^{60}Co, which has a half life of 1925.28(14) days, and emits characteristic γ-rays at 1173.228(3) and 1332.492(4) keV. The branching ratio for the two emmitted γ-rays is assumed to be

$$br(1173.228 \text{ keV}) \approxeq br(1332.492 \text{ keV}) \approxeq 1. \tag{3.7}$$

Table 3.3: Absolute efficiency measured using a 1.9% calibrated ^{60}Co source set 10.5 cm above the GEARS detector. The spectrum used to determine the photopeak counts is shown in Fig. 3.3.

Energy (keV)	Photopeak counts	A(t_0) [Bq]	t-t_0 [d]	τ [d]	t_{live}[s]	$\epsilon_{abs.}$[%]
1173.228	216502(637)	15429(295)	59	2777.59(20)	7297	0.196(4)
1332.492	197751(597)					0.179(3)

The error in absolute efficiency, $\delta_{\epsilon_{abs.}}$ is given by Eq. 3.8 and results from having a high activity source and a long measurement time to ensure that the measurement can have high counting statistics, and the error in the activity, δ_A is the dominating factor [16].

$$\frac{\delta_{\epsilon_{abs.}}(E_\gamma)}{\epsilon(E_\gamma)} = \frac{\delta_A(t_0)}{A(t_0)}. \tag{3.8}$$

Table 3.4: Absolute and relative detection efficiencies for characteristic ^{60}Co γ-ray energies.

Energy (keV)	ϵ_{abs} [%]	$\epsilon_{rel.}$ [arb.]
1173.228	0.196(4)	361(30)
1332.492	0.179(3)	330(28)

The relative efficiency curve can then by scaled to the absolute efficiency following

$$\epsilon_{abs.}(E_\gamma) = S \cdot \epsilon_{rel.}, \tag{3.9}$$

where $\epsilon_{rel.}$ is calculated according to Eq. 3.4 using parameters from Table 3.2, and S is a scaling factor, calculated according to Eq. 3.10. $\epsilon_{\text{ref.}}$ and $\epsilon_{\text{abs.}}$ for ^{60}Co are shown in Table 3.4.

$$\begin{aligned} S &= \frac{(\epsilon_{rel.1173 \text{ keV}})(\epsilon_{abs.1173 \text{ keV}}) + (\epsilon_{rel.1332 \text{ keV}})(\epsilon_{abs.1332 \text{ keV}})}{\epsilon^2_{rel.1173 \text{ keV}} + \epsilon^2_{rel.1332 \text{ keV}}} \\ S &= 0.00000544(8) \end{aligned} \tag{3.10}$$

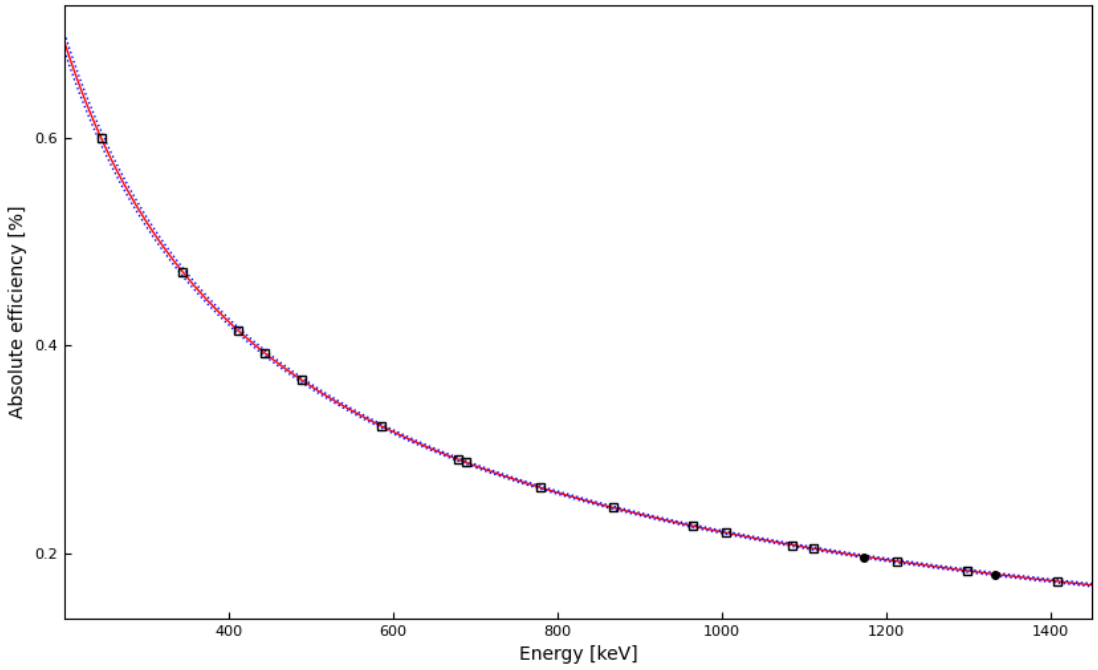

Figure 3.6: Efficiency calibration of GEARS performed using a ^{152}Eu and ^{60}Co source. Best fit line is shown in red, while blue dotted line indicates the confidence interval, established using method described in Appendix B. Empty squares show ^{152}Eu data points, and filled circles show ^{60}Co data points. Error bars are smaller than the data points.

The absolute efficiency curve for GEARS is shown in Fig. 3.6. It is important to note that the absolute efficiency has been calculated for a point source sitting 10.5 cm above the detection can. This means that samples with a different geometry will have slightly different detection efficiency depending on where they are placed respective to the detection can, and due to the geometry of the sample itself.

3.3 Time resolved energy peak fitting

Once GEARS has been calibrated, samples with unknown activity, lifetime, or composition can be measured in order to determine these parameters. For this thesis, the unknown quantity of interest is the activity, as the lifetime and isotopic composition of the samples are already known. For long detection times when $t_{live} \gg \tau$, the activity of a source can be determined by observing the number of counts detected over the length of the run, using a time resolved spectrum. To calculate the activity of the source at the beginning of the run, the number of γ-rays detected follows Eq. 2.1. The number of γ-rays detected, P_i, during the time interval Δt at time t_i is given by integrating Eq. 2.1 to give

$$
\begin{aligned}
P_i &= \int_{t_i}^{t_i+\Delta t} P(t)dt \\
&= P_0 e^{-\lambda t_i}\left(1 - e^{-\lambda \Delta t}\right).
\end{aligned}
\tag{3.11}
$$

Background is also detected, which can be modeled as a second order polynomial following

$$
B(t) = b_0 + b_1 t + b_2 t^2, \tag{3.12}
$$

and the number of detected counts due to background in the time interval Δt at time t_i is given by

$$
\begin{aligned}
B_i &= \int_{t_i}^{t_i+\Delta t} B(t)dt \\
&= b_0 \Delta t + b_1 \left(\Delta t \cdot t_i + \frac{\Delta t^2}{2}\right) + b_2 \left(\Delta t \cdot t_i^2 + \Delta t^2 \cdot t_i + \frac{\Delta t^3}{3}\right).
\end{aligned}
\tag{3.13}
$$

In order to model the total number of events in a time resolved peak, the sum of the background and γ-rays originating from the source are added together. The total number of counts is thus the sum of Eq. 3.11 and Eq. 3.13 to give

$$
\Sigma_i = P_i + B_i, \tag{3.14}
$$

where the 4 free parameters are P_0, b_0, b_1 and b_2. In order to ensure a proper fit, the background is fit simultaneously by fitting B_i to a time resolved region of the spectrum that is higher in energy than the peak and only consists of background. The parameters can be solved following the least squares method outlined in Appendix C. Once P_0 has been determined, the true activity of the source at the beginning of the run, A_0, is calculated following

$$
A_0 = \frac{\lambda P_0}{\epsilon_{\text{abs.}}(E_\gamma)}, \tag{3.15}
$$

where P_0 is equal to N_0, the number of radioactive nuclei in the source at the beginning of the measurement. The exponential law of radioactive decay, Eq. 2.1, can now be rewritten for activity following

$$
A(t) = A_0 e^{-\lambda t}, \tag{3.16}
$$

in order to calculate the activity of the sample at any point in time after its creation.

Chapter 4

Neutron induced isotope production

Part of the NSL experimental program is the production of radioisotopes using the neutron generator facility. This chapter will outline the plans for the development of an isotope production device in response to the global shortage of medical isotopes. More specifically, this chapter will begin with an overview of the current Technetium-99m (^{99m}Tc) isotope supply chain, followed by the basics of neutron interactions, information about the neutron generator facility, and experimental studies that have been completed for the development of the isotope producer. This chapter will conclude with an outlook on future studies for the processing of isotopes produced by neutron bombardment and scalability of the isotope production device.

4.1 ^{99m}Tc supply chain

^{99m}Tc is the most widely used radioisotope in medical diagnostic procedures. It is a metastable isomer of technetium-99 (^{99}Tc) with a half life of ∼6 h, and is used for diagnostic imaging of organ function [17]. ^{99m}Tc emits a 140 keV γ-ray when it decays to ^{99}Tc, which is a sufficient energy for passing through the human body and detection by a γ-ray detector, while being low enough energy such that it does not resut in excessive radiation dose to the patient. Furthermore, it can be easily tagged to chemical tracers in order to target specific organs or tissues when injected into the human body [18].

The predominant method of ^{99m}Tc production does not produce ^{99m}Tc directly, opting to produce the parent ^{99}Mo instead. ^{99}Mo decays into ^{99m}Tc with a 66 h half life, which is long enough to allow for chemical processing and distribution before the activity decays. ^{99}Mo is made in nuclear reactors from the irradiation of uranium targets using thermal neutrons, which have characteristic energy equal to 0.025 eV. The interaction of neutrons with uranium-235 (^{235}U) nuclei result in a fission reaction, and the production of heavy and light fission fragments, one of which is ^{99}Mo [19]. Targets are irradiated for 5 - 7 days

depending on the geometry of the target and neutron flux of the reactor, in order to reach the saturation amount of ^{99}Mo [20]. Once the targets are removed from the reactor, they

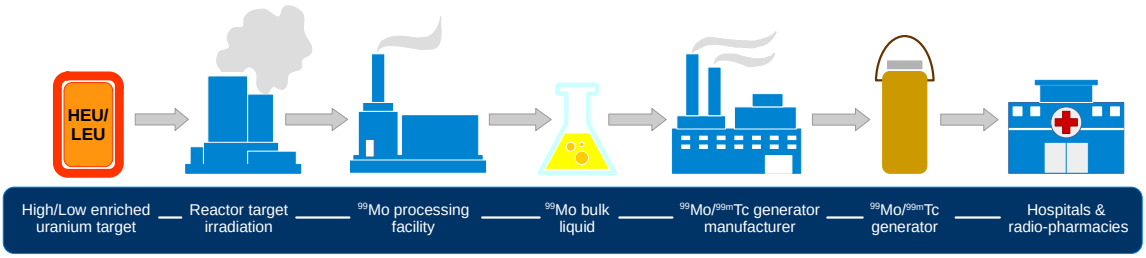

Figure 4.1: A diagram of the ^{99m}Tc supply chain. The supply chain begins with the irradiation of enriched uranium targets within nuclear reactors. The targets are then processed to isolate the ^{99}Mo, which is put into ^{99m}Tc/^{99}Mo generators, and distributed to hospitals and radiopharmacies.

In 2009-2010 there was an isotope supply crisis in which the world experienced a shortage, resulting in cancellation of medical procedures or alternative isotopes being used. Although there are alternatives for many standard procedures, they often come with problems that result in any substitutes being less than desirable. Common alternatives are: (i) fluorine-18 (^{18}F) which is lacking supportive infrastructure [24]; (ii) thallium-201 (^{201}Tl) which gives a higher radiation dose to the patient [25]; and (iii) rubidium-82 (^{82}Rb) which is not licensed in all jurisdictions [26]. Alternative detection devices can also be used, but they are often already in high demand and are unable to accomodate the additional procedures [27, 28]. The ^{99m}Tc shortage was in part due to the fact that there were only 5 reactors, all over 40 years old, supplying the world's demand of ^{99}Mo [29]. As two of the largest suppliers went into unplanned shutdowns for maintenance, the remaining suppliers were unable to increase their supply to meet the demand. Since then, Poland, Czech Republic, and Russia contributed their old research reactors to the supply chain. However, two of the historically largest contributors, France and Canada, stopped contributing as their reactors were decommissioned thus decreasing the world's total annual supply. As of 2019, the world's supply of ^{99}Mo is split between 9 producers shown in Table 4.1 [27]. Of the reactors listed, the majority of them are over 50 years old, which is much longer than the expected lifetime of a reactor (20-30 years), with Australia being the most recent contributor [30].

Although the crisis was averted following 2010, it is apparent that an unplanned disruption could severely cripple the supply chain. More recently, a disruption occurred in 2020, due to the COVID-19 pandemic that resulted in the shutdown of borders and air transportation causing bottlenecks in transportation and distribution [31, 32]. Facilities have continued production under COVID-19 safety protocols, including social distancing, as they are considered essential services, but with the difficulties in distribution, medical procedures are still being cancelled due to the lack of ^{99}Mo and, by extension, ^{99m}Tc.

Table 4.1: A table consisting of nuclear research reactors contributing to the world's supply of ^{99}Mo as of 2019 [27].

Reactor Name	**Country**	**Year Commissioned**	**Share of annual total world production**
ANSTO (OPAL)	Australia	2007	16%
CNEA (RA-3)	Argentina	1967	2%
NCBJ (MARIA)	Poland	1974	9%
NECSA (SAFARI-1)	South Africa	1965	14%
NRG (HFR-Petten)	Netherlands	1961	26%
RC Rex (LVR-15)	Czech Republic	1995	10%
Rosatom (RIAR and KARPOV)	Russian Federation	1961-1984	5%
SCK-CEN (BR-2)	Belgium	1963	15%
University of Missouri (MURR)	United States	1966	4%

In developing a permanent solution, three main points that need to be addressed are the use of uranium, the cost of irradiation and the final product, and the impact of having few facilities around the world providing services for the entire global population [33]. A relatively new approach that would address these issues is by targeting the ^{100}Mo (p,2n)^{99m}Tc reaction by irradiating isotopically enriched ^{100}Mo with protons using a cyclotron [34]. This method is shown to be promising, in that a high-current, medium energy medical cyclotron can produce up to 1.4 TBq of ^{99m}Tc within its 6 hour half life. This quantity is large enough to satisfy the demand for a large metropolitan area, providing the product is isotopically and chemically pure enough [35]. This method is advantageous because as well as removing the need for a nuclear reactor, it also removes the radioactive waste associated with the use of uranium targets and fission products. However, new problems arise from this approach as the amount of Mo produced by a single cyclotron is much lower than that produced by reactors.

An alternative method of production that would address the issues outlined above, help subsidize the worlds supply, and diversify the type of supplier is to use a neutron generator for neutron activation of a target. The D-T NG housed at SFU emits high energy neutrons (14.1 MeV), which induce neutron reactions when interacting with a target. Neutron activation of ^{102}Ru can result in the absorption of a neutron (n) followed by the emission

of an alpha particle to produce ^{99}Mo. Following irradiation, the resulting ^{99}Mo can then be chemically separated from the bulk target with the goal of producing isotopically pure ^{99}Mo with high specific activity. This method of production would remove the requirement for uranium targets and irradiation within nuclear reactors. In addition, the resulting product will be able to be fed into the current supply chain in order to take advantage of the preexisting infrastructure.

4.2 Neutron generator facility

(a) (b)

Figure 4.2: The image on the left, 4.2a, shows the neutron generator facility set up with the neutron generator linear accelerator in the corner and the power supply on the bench. Figure 4.2b shows the beam tube set up in a stand, with a sample placed along the line of optimal irradiation.

The neutron generator facility at SFU is located in the C7076 vault of the Chemistry building. It holds a Thermo Scientific P-385 neutron generator [36] with the full set up shown in Fig. 4.2a, and the linear accelerator shown in Fig. 4.2b. Neutrons are produced from the following reaction:

$$^{2}\mathrm{H} + ^{3}\mathrm{H} \rightarrow \mathrm{n} + ^{4}\mathrm{He}, \qquad \mathrm{Q}{=}17.590\mathrm{MeV}. \tag{4.1}$$

The neutrons produced from this reaction are fast neutrons with 14.1 MeV energy, and a nominal flux of 3×10^8 neutrons per second as specified by the supplier. The neutron generator is guaranteeed to be able to operate at full flux for 1500 hours, after which operation at the quoted neutron flux is not guaranteed. The Q-value given is the energy released during the reaction due to the difference in rest mass energy between the reactants and products. The location of the neutron generator within the vault has been determined via a series of tests to minimize the dose acquired by people working in the surrounding areas [37].

4.3 Neutron interactions with matter

The amount of product that can be expected to be produced during a neutron activation experiment can be predicted based on the composition of the sample, and the energy and flux of the neutrons being used providing the interactions of neutrons with the target materials is understood. This section will discuss the manner in which neutrons interact with materials being activated which are relevant to the neutron activation experiments carried out in this study.

Nuclear reactions are typically written as [2]

$$a + X \rightarrow Y + b, \tag{4.2}$$

where a is the projectile, X is the target, and Y and b are the reaction products. Usually, Y is a heavy product and y is a light particle that can be detected. The type of reaction occurring is classified by Y and b. Only neutron interactions where $a = n$ will be discussed, as the projectiles used for the isotope producer project are high energy neutrons produced from the NG.

Reactions can be classified as either *direct reactions*, in which only a single nucleon has time to interact while a and X are in range of one another, or *compound reactions*, in which a large number of interactions between nucleons can occur while a and X are in range of one another. Direct reactions are convenient for studying nuclear interactions because they can accurately be described as single step transitions from the initial to final states [38]. Examples of direct reactions are stripping, pickup, breakup, and knock-out. In a stripping reaction, a nucleon is transferred from the projectile to the target. Conversely, during a pickup reaction a nucleon is transferred from the target to the projectile. A breakup reaction occurs when the projectile breaks up into separate nuclei, and a knock-out reaction occurs when a single nucleon or a small cluster of nucleons is removed from either the projectile or target during their interaction. The reaction of interest for this thesis is the knock-out reaction. For the isotope producer project, isotopes will be produced as a result of a knock-out reaction in which a small cluster of nucleons is removed during the interaction

to produce an alpha particle [2]. To reflect the knock-out reaction as a result of an incoming neutron and the knock-out of an α particle, Eq. 4.2 will be rewritten as

$$n + X \rightarrow Y + \alpha, \tag{4.3}$$

which can be shortened to the following form,

$$X(n, \alpha)Y, \tag{4.4}$$

and will henceforth be referred to as an (n, α) reaction.

4.4 Neutr

The NG can be
in which a samp
result can be th
written as (n, x)
of the advantage
target is negligib
bulk sample [39]

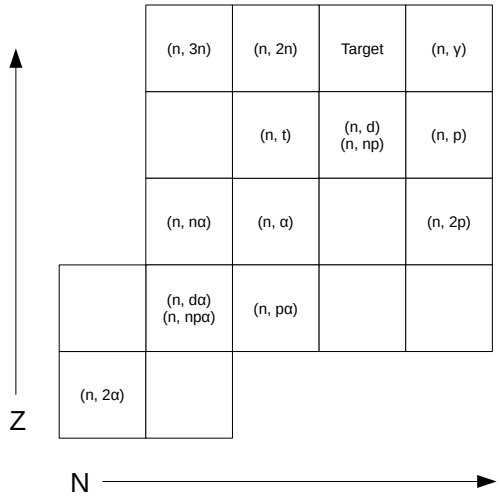

Figure 4.3: Figure shows (n, x) reactions that can occur during neutron activation, relevant to the isotope producer experiment.

Due to the non-destructive nature of neutron activation it is an ideal technique for studying sensitive samples, such as those used in archaeology and geology, in order to determine their elemental composition [40]. It is also ideal for producing radioisotopes, as the same target can be used almost indefinitely.

4.4.1 Reaction Kinetics

The reaction kinetics for the neutron interactions with the target material during and after irradiation can be determined by calculating the reaction rate, R, following

$$R = \phi_n N_t \sigma, \tag{4.5}$$

where ϕ_n is the neutron flux through the targets surface area, N_t is the total number of target nuclei in the irradiated sample, and σ is the interaction cross section. The nuclear cross section depends on the energy of the neutrons and the properties of the target nucleus. The reaction rate is the number of radioactive product nuclei being produced per unit time, and thus the amount of radioactive nuclei present increases as the length of the irradiation increases. Once the radioactive nuclei are produced, they will begin to decay and produce daughter nuclei, thus decreasing the number of product nuclei in the sample. The change in the number of radioactive nuclei at any given point in time can be calculated according to

$$\frac{dN_p}{dt} = R - \lambda N_p, \tag{4.6}$$

where N_p is the number of radioactive product nuclei. Eq. 4.6 can be solved as a simple ordinary differential equation (ODE), making the assumption that the initial activity of the sample is equal to 0, to give number of radioactive nuclei as a function of time during irradiation as

$$N(t_{irr.}) = \frac{R}{\lambda}(1 - e^{-\lambda t_{irr.}}). \tag{4.7}$$

The activity of the produced radioactive nuclei given by $A(t_{irr.})$ is defined by the relationship between the number of radioactive nuclei and the activity as previously defined in Eq. 2.3 to give

$$A(t_{irr.}) = R(1 - e^{-\lambda t_{irr.}}) \tag{4.8}$$

The reaction kinetics for neutron interactions with a target material is shown in Fig. 4.4.

During irradiation, the activity will build towards a saturation activity equal to R, however it will never achieve or surpass R. Once the irradiation has stopped, the number of product nuclei will decrease due to radioactive decay following

$$A(t_{p.i.}) = A_0 e^{-\lambda t_{p.i.}}, \tag{4.9}$$

where $t_{p.i.}$ is the time that has passed, post irradiation.

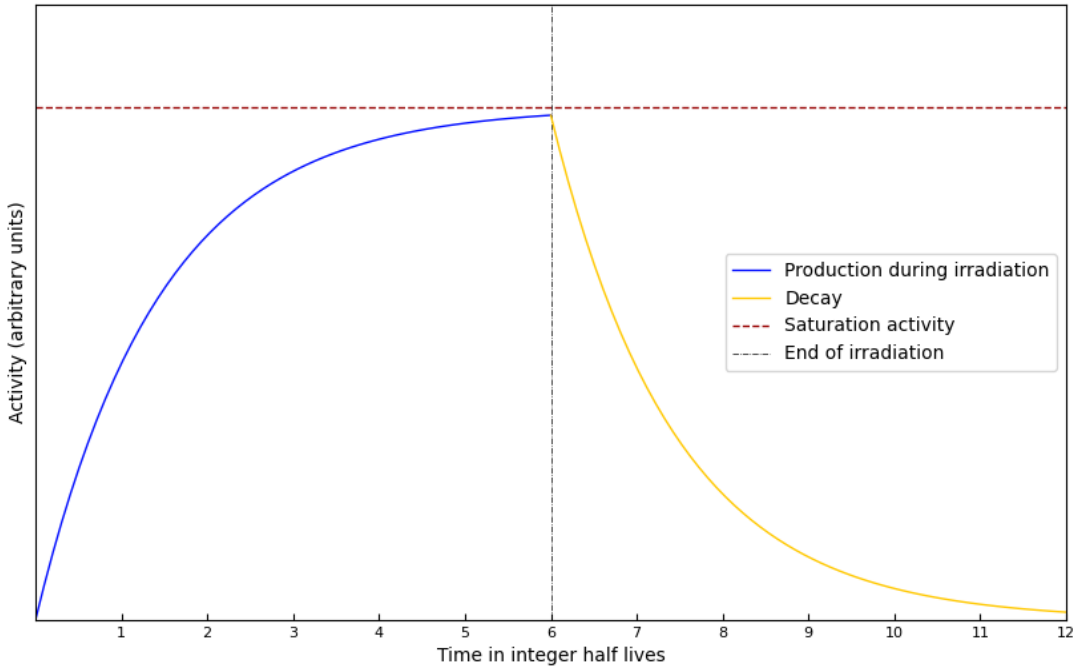

Figure 4.4: Figure shows an example of an activity curve for a radioactive isotope during and after irradiation. The blue curve shows the increasing activity as during irradiation, while the yellow curve shows the decrease in activity once the generator has been turned off. Saturation activity is shown by the dotted red line, and the black line indicates the point in time the generator is turned off.

4.5 Beer-Lambert's law

When neutrons move through a target mass they are attenuated as they interact with target nuclei. This attenuation results in fewer neutrons being available for interactions as the neutron population continues to move through the target. The attenuation of a population of neutrons moving through matter is modeled using Beer-Lamberts law which says that the neutron flux (φ) will be attenuated by an attenuating factor, μ, such that

$$\frac{d\varphi(z)}{dz} = -\mu \cdot \varphi(z) \tag{4.10}$$

where μ is a property of the target material. This first order differential equation can be solved following

$$\begin{aligned} \int_0^z \frac{1}{\varphi(z)} d\varphi(z) &= \int_0^z -\mu dz \\ ln(\varphi(z)) - ln(\varphi_0) &= -\mu z \\ \varphi(z) &= \varphi_0 e^{-\mu z}, \end{aligned} \tag{4.11}$$

where z is the thickness of the attenuating material. For neutrons, the attenuating factor is equal to

$$\mu = \frac{1}{L} \tag{4.12}$$

where L is the mean free path, and is defined as the average distance traveled by a particle between interactions. The mean free path is unique to the matter being traversed by the neutrons, and depends on the number density of nuclei within the sample, η, and the interaction cross section, σ, such that

$$\frac{1}{L} = \eta \cdot \sigma. \tag{4.13}$$

For inhomogeneous samples, the attenuation coefficient and the mean free path for the given sample is dependent on all constituents, where the total mean free path, L_t is related to the mean free path of each individual constituent, following

$$\frac{1}{L_t} = \sum_i \frac{1}{L_i} \tag{4.14}$$

for all elements, i, that make up the target. The cross section is unique for each element and can be found on the National Nuclear Data Center website for any specific interaction [15]. When calculating the mean free path through a target in order to determine the change in φ, it is important to use the (n, total) cross section, as the interaction of neutrons in any capacity can cause attenuation. Although every interaction may not remove the neutron from the target, the attenuated neutrons will have a decreased energy and will be moving in a different trajectory. Equation 4.11 can now be rewritten in terms of the mean free path as

$$\varphi(z) = \varphi_0 e^{-\frac{z}{L_t}}. \tag{4.15}$$

This behaviour is modeled in Fig. 4.5, which shows that the neutron flux is attenuated by a factor of $1/e^L$, for integer values of L, as they move through media.

4.6 Szilard-Chalmers reaction

Once the isotope is produced, an effective separation process is required for purification of the product in order for it to be useful. Chemical separation of different elements is possible due to the difference in chemical behaviour. A chemical difference can be achieved by producing a different element altogether, or by changing the chemical environment of the original target such that recoiling product nuclei will form chemically separable molecules [41].

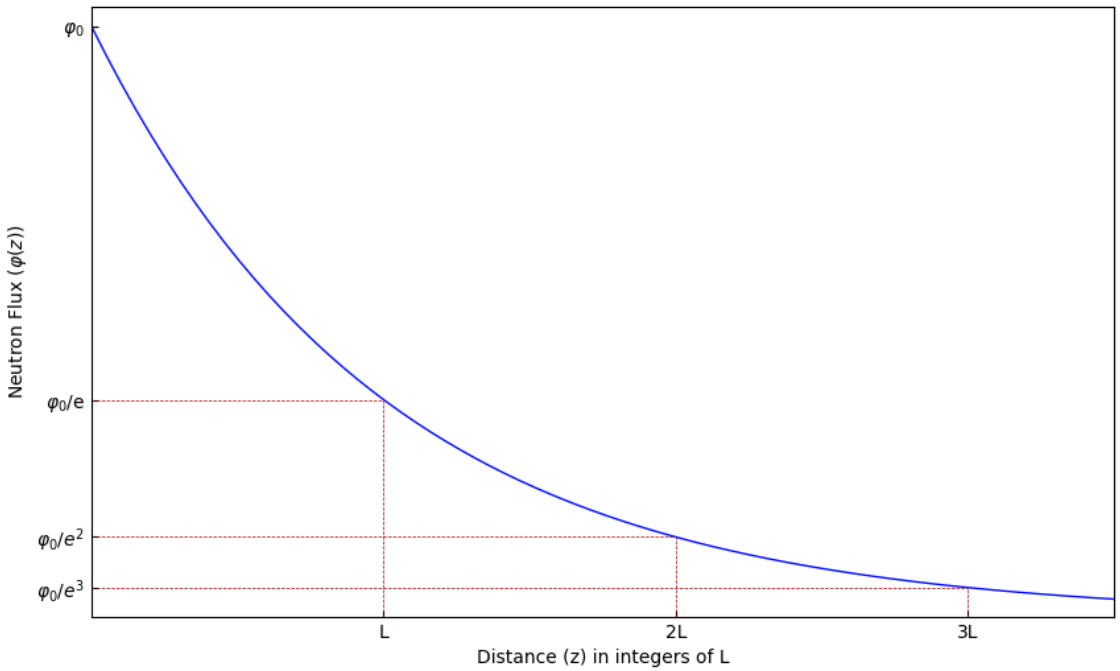

Figure 4.5: Neutron attenuation following Beer-Lamberts law shows a decrease in original neutron flux (φ_0) proportional to $1/e^L$ as the population travels integer values of L through the target material.

The first step in addressing the separation process, is by taking advantage of the Szilard-Chalmers reaction. Discovered in 1934, Szilard and Chalmers used thermal neutrons in order to induce an (n, γ) reaction [42]. Upon the emission of the gamma ray, due to conservation of energy and momentum, there was enough energy imparted upon the nucleus in order to overcome the intermolecular forces holding the molecule together, thus separating the product from the initial target. This reaction is not unique to gamma emission, and can result from the emission of α and β particles from a nucleus, or during the absorption of nucleons, such as neutrons or protons, into a nucleus. This behaviour will henceforth be referred to as nuclear recoil [43].

Following the observation of this reaction, Szilard and Chalmers were able to achieve a 50% separation from the recoil. In theory, due to the relative energy of the emitted γ-ray (10^2 eV range) and the intermolecular forces (eV range), it was hypothesized that the separation should be 100% effective. The reason for the decreased separation ratio is due to the stopping distance of the resulting nuclei as it moved through the target medium. When the nucleus is freed from the molecular structure it loses electrons depending on the speed at which it is travelling, resulting in a positive charge. As the positively charged nucleus moves through the target, it loses energy through interactions with other atoms. The distance between the start of the recoil, and the point at which the energy of the positively charged particle is almost zero is defined as the range [44]. If the range of the

nucleus is shorter than the distance from start of the recoil to the edge of the target, the nucleus will recombine resulting in retention of the product nucleus within the target.

For the isotope production experiment, the reaction mechanism is an (n, α) reaction. This differs from the Szilard-Chalmers reaction in that they were observing a recoil only due to γ-decay. For this study, recoil can occur at two instances; during the neutron bombardment of the sample, and upon emission of an alpha particle. The advantages of using the (n, α) reaction in comparison to the (n, γ) reaction used by Szilard and Chalmers, is that the neutron imparted energy on the order of MeV, while the α particle imparted energy on the order keV. During the Szilard-Chalmers reaction, the impacting neutron only had an energy on the order of eV, while the γ-ray imparted a recoil energy on the order of 10^2 eV range. The calculation of recoil energies resulting from (n, α) reactions with 14.1 MeV neutrons is shown in Appendix F.

Chapter 5

Isotope Producer Experimental Design

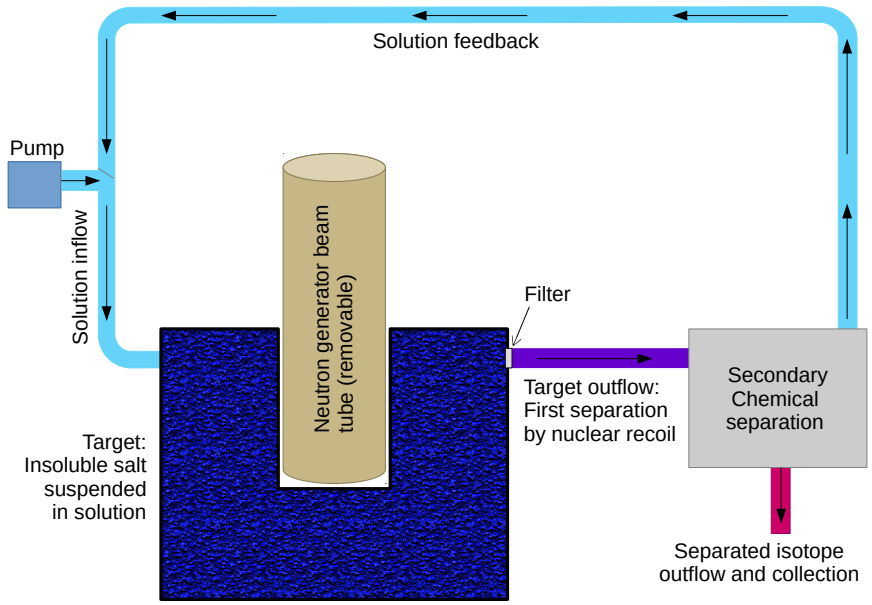

Figure 5.1: A schematic of the proposed device for the isotope producer is shown. Components of this device are the neutron generator set within a tank filled with target material and a circulatory pump. The pump forces solution through the tank and out through a filter. It is then circulated back into the tank after it has gone through the chemical separation component.

Neutron induced isotope production will take advantage of the Szilard-Chalmers reaction, and the non-destructive nature of neutron activation. In order to do this the sample used for irradiation will have the target nuclei in form of salts or grains suspended within a solution so that the product can recoil out of the target grain and be suspended in a

solution, allowing for a simple separation process. The proposed device consists of a tank filled with the target grains suspended in solution, constructed with a cavity for the neutron generator to be placed into such that the point of neutron emission occurs at the center of the sample. The first pass separation would be a filtration to separate the products in the solution from the bulk target, followed by a secondary chemical separation stage to purify the isotope. The separated isotope can be collected and processed for the appropriate use. The remaining solution can be cycled back to the target by way of a circulatory pump to keep the solution flowing. Some type of perturbation in the target tank would be required to ensure that the target grains remain suspended in solution and do not settle at the bottom. A schematic of the device is shown in Fig. 5.1.

The first step in realizing the isotope producer is determining the appropriate target size, and the ideal composition ratio of grains to solution. The ideal target size will be determined by the decrease in neutron flux due to reactions occurring as the target size increases and can be determined analytically for different target geometries. The composition ratio is constrained by the requirement that the solution must be able to flow through the grains and will be determined experimentally. In order to model the behaviour of an irradiated sample, for preliminary analytical studies a spherical target geometry has been chosen, with a neutron point source in the center of the target to approximate the neutron generator resting within a tank of the target, as shown in Fig. 5.2. Using the spherical model, the loss of neutrons through the target, or the reaction rate, can be determined analytically for varying neutron flux, target size, and target composition ratios in order to optimize the target. A spherical geometry has been chosen for a multitude of reasons. Neutrons are emitted isotropically and as such the most efficient set up for maximizing the amount of reactions occurring, and consequently the amount of product, would be to have the target completely surrounding the neutron source with a spherical shape. Additionally, the spherical geometry is convenient for calculations, and can be used as a reference for creating future simulations of more sophisticated geometries.

When doing preliminary calculations for the target parameters, the spherical target is discretized. The reasoning behind the discretization is to determine the reaction rate in each layer of thickness, dr, of increasing inner radius, r, in order to determine the impact of an increasing target size on the number of reactions occurring. By studying the effects of incrementally increasing the size of the target, an ideal size can be determined that maximizes the ratio of the number of nuclei of interest to the rest of the nuclei in the target. The first calculation done is to determine the reaction rate in each layer of the sphere.

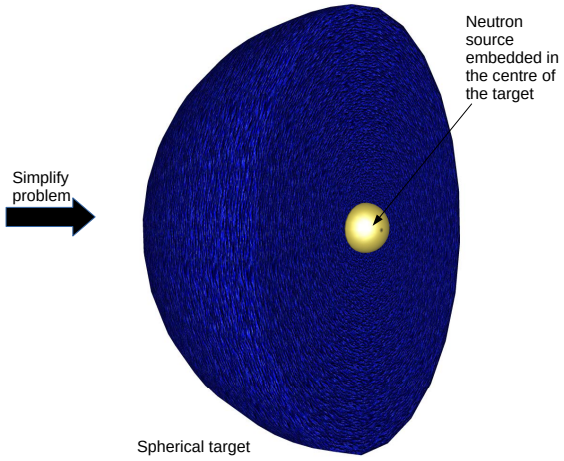

Figure 5.2: The spherical model that is used for preliminary calculations is shown. The neutron source embedded in the center emits isotropically with a flux of 3×10^8 neutrons/s at 14.1 MeV. The spherical target consists of grains suspended in solution.

5.1 Nuclei in the target material

In order to calculate the reaction rate, the number of reactants, neutrons and target nuclei, need to be known. As previously discussed in Sec. 4.5, the number of neutrons can be determined once the mean free path is known, and in order to determine the mean free path, the target composition and nuclear density is required. The mean free path of neutrons through each individual element is different, so it is important to determine the number of nuclei of each unique element in order to calculate the true reaction rate. First, the total volume of the target is established to be comprised of the insoluble grains and the solvent following

$$V_T = V_g + V_s, \tag{5.1}$$

where V_T is the total volume of the target, V_g is the volume of the grains, and V_s is the volume of the solvent. The volume of grains is related to the total volume by defining the volume ratio, V_R, as

$$V_R = \frac{V_g}{V_T}, \tag{5.2}$$

The volumes of grain and solvent are related to the volume ratio by

$$V_g = V_R V_T, \quad \text{and} \quad V_s = (1 - V_R)V_T. \tag{5.3}$$

The volume ratio is a convenient parameter to define for optimization studies of the ideal ratio of grain to solvent for the target. Another important relationship to define is between the mass and volume of the target components, as it is convenient to weigh the sample

rather than determine the volume being used when preparing the samples. The relationship between mass and volume for any compound, j, is given by

$$V_j = \frac{m_j}{\rho_j}, \tag{5.4}$$

where ρ is the density. The masses of the grains and solvent are expressed as

$$m_g = \rho_g V_R V_T, \quad \text{and} \quad m_s = \rho_s (1 - V_R) V_T. \tag{5.5}$$

This definition of the grain mass and solvent mass is the most convenient way to relate the masses of the target components to the volume of the target, as the exact amount of each can be weighed out and used once a volume ratio and total volume has been chosen. Furthermore, the constraints on target composition are imposed by the volume ratio. In order to maximize the number of reaction products, the number of grains need to be maximized. However, the target still needs to be able to be stirred so that the grains remain suspended in the solution without settling.

The density of each target component can be used to determine the number of nuclei in each consecutive layer of the spherical target, following

$$\varrho_j = \frac{\rho_j N_A}{M_j}, \tag{5.6}$$

where ϱ_j is the molecular number density of the target component in units of molecules/cm^3, N_A is Avogadros number, and M_j is the molar mass of the target component. The number of nuclei for each element in the volume can then be determined using the number of atoms of a unique element within a molecule to give the number density of nuclei as

$$\eta_j = Ab_j \kappa_j \varrho_j, \tag{5.7}$$

where η_j, Ab, and κ_j is the number density, abundance, and number of atoms of element j in the molecule, respectively. The total number of nuclei of an element j, N_j in a volume, dV, can be calculated for all target components following

$$\begin{aligned} N_{j,g} &= \eta_{j,g} V_R dV \\ N_{j,s} &= \eta_{j,s} (1 - V_R) dV, \end{aligned} \tag{5.8}$$

where the second subscripts g and s denote the constituent nuclei belonging to atoms in the grains and solvent, respectively. The volume element is a spherical shell of thickness dr equal to

$$dV = 4\pi r^2 dr. \tag{5.9}$$

5.2 Neutron flux

Once the target composition is known, the neutron flux through the target can be calculated. For the chosen geometry of the target and neutron point source shown in Fig. 5.2, the neutron flux through the surrounding spherical target, $\phi(r)$ is related to the total number of neutrons emitted by the neutron source following

$$\phi(r) = \frac{\varphi(r)}{4\pi r^2} \tag{5.10}$$

where the surface area of a sphere of radius r is equal to the denominator on the right hand side of Eq. 5.10, and neutron flux is given in units of $(\frac{neutrons}{s \cdot cm^2})$. In order to determine the flux through the chosen target, the mean free path of neutrons through the target needs to be calculated, as seen in Eq. 4.15. For the nonhomogeneous target discussed in Sec. 5.1, the mean free path of the target is calculated according to Eq. 4.14, which takes into account the mean free path of neutrons through each constituent element within the target according to Eq. 4.13. The number density of each nuclei is determined as shown in Eq. 5.7 and the (n, total) cross section is used for each constituent nuclei, resulting in the final expression for the mean free path of neutrons through a nonhomogeneous target as seen in Eq. 5.11

$$\frac{1}{L_t} = \sum_j \eta_{n_j,g} \sigma_{n_j,t} V_R + \sum_j \eta_{n_j,s} \sigma_{n_j,t} (1 - V_R). \tag{5.11}$$

5.3 Reaction rate of isotope production

The reaction rate of isotope production within the discretized target can now be calculated using the neutrons flux as shown in Eq. 5.10, and the sum of the number of nuclei of the constituent target components and their (n, total) cross sections. Eq. 4.5 is thus rewritten to give the reaction rate, R_t, as

$$R_t = \phi(r) \sum N_j \cdot \sigma_{j,t}. \tag{5.12}$$

Substituting the expression for neutron flux as in Eq. 5.10, and noting that the sum of all $N_j \cdot \sigma_{n_j,t}$ can be rewritten in terms of the mean free path from Eq. 5.11, the reaction rate can be rewritten as

$$\begin{aligned} R_t(r) &= \frac{\varphi(r)}{4\pi r^2} \frac{4\pi r^2}{L_t} dr \\ R_t(r) &= \frac{\varphi(r)}{L_t} dr. \end{aligned} \tag{5.13}$$

It is now evident that due to the choice in geometry, the increase in the number of target nuclei in each consecutive spherical layer of the target with inner radius r, and thickness dr is directly compensated by the decrease in the neutron flux as the inner radius and thus

inner suface area of the spherical layer increases in size. Finally, in order to calculate the reaction rate in each spherical shell, Eq. 5.13 can be integrated between the limits of r and $r + dr$ to give

$$\begin{aligned} R_t(r, r+dr) &= \int_r^{r+dr} \frac{\varphi(r)}{L_t} dr \\ &= \varphi(r) - \varphi(r+dr). \end{aligned} \tag{5.14}$$

Using the full expression for $\varphi(r)$, as shown in Eq. 4.11, the reaction rate in each spherical shell of thickness dr, with inner radius r is given by

$$R_t(r, r+dr) = \varphi_0 e^{-\frac{r}{L_t}} \left(1 - e^{-\frac{dr}{L_t}}\right). \tag{5.15}$$

This result is expected, as the attenuation of neutrons is calculated using the (n, total) cross section, which implies that the loss of neutrons is the result of a reaction occurring. The number of reactions is thus equal to the difference in the number of neutrons in the sphere at the inner and outer surface of the spherical volume element.

5.4 Branching Ratio

During the neutron bombardment, any number of (n, x) reactions can occur, and the reaction rate includes all possible reactions. In order to determine the number of reactions of interest, or (n, α) reactions occurring, a branching ratio, br, is defined as

$$br = \frac{L_t}{L_{int.}}, \tag{5.16}$$

where $L_{int.}$ is the mean free path for reactions of interest, in this case the (n, α) reaction, and $R_{int.}$ is the reaction rate for the reactions of interest. br is used to determine the probable ratio of (n, α) reactions to (n, total) reactions occurring within the target, and is used to calculate the number of reactions of interest, $R_{int.}$, following

$$R_{int.} = br \cdot R_t. \tag{5.17}$$

Finally, the amount of product that can be expected to be produced using the target and neutron source as shown in Fig. 5.2 can be calculated. These calculations will be used as a preliminary test for determining whether or not a reaction is viable for producing appreciable amounts of an isotope.

Chapter 6

Isotope Producer Experimental Results

A series of experiments was undertaken in order to prove the viability of the proposed isotope producer as an isotope production method. First, a target composition optimization experiment was carried out to establish the volume ratio, which was then used to determine the mean free path of a ^{nat}Ru in water target, and ^{27}Al in water target. In Sec. 6.2, the viability of the isotope producer for the production of ^{99m}Tc will be estimated by using the determined volume ratio to calculate the reaction rate using various NG's. Upon achieving satisfying results, the reaction rate for the production of ^{24}Na was calculated to show its viability as a cheap, convenient reaction to study for preliminary experiments and development of the isotope producer. The Szilard-Chalmers recoil separation efficiency was also tested by irradiating a target of ^{27}Al in water using the NG at the NSL, centrifuging the sample, and decanting the liquid to determine how much of the ^{24}Na had separated out of the grains and into the solution. Results of these experiments will be shown and discussed.

6.1 Target composition optimization

The target composition is optimized for a given volume ratio by calculating the corresponding mean free path and reaction rate. To choose the ideal volume ratio, a simple experiment was performed using neutral alumina purchased from Thermo Fisher Scientific for the grains, and city of Burnaby, British Columbia tap water as the solvent [45]. The water was added to a beaker containing alumina and a magnetic stirring rod rotated to achieve a small vortex. The beaker was weighed without alumina, with alumina, and then again with the water added in order to determine the amount of water added. This is shown in Fig. 6.1, with the achieved ratio being 20% target grains to 80% solvent, or $X_V = 0.2$.

Using the determined volume ratio, the reaction rate is calculated following Eq. 5.15 for an increasing target radius to see how rate changes as the spherical target radius increases in increments of *dr*. The target size is restricted by the requirement that the reaction rate for

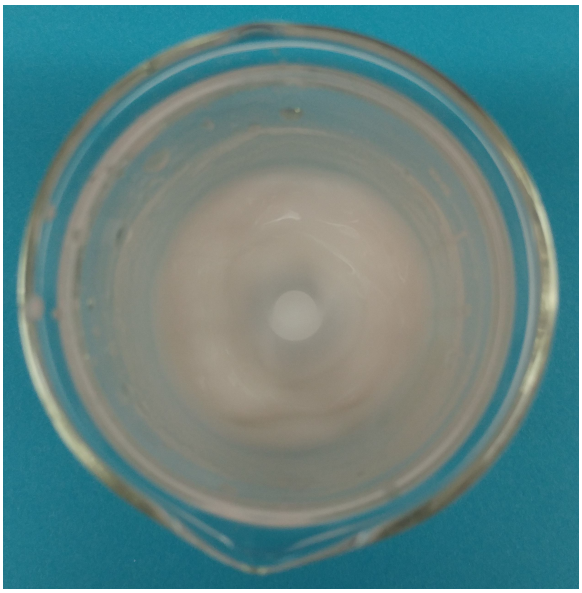

Figure 6.1: This image shows a mixture of alumina in water, with a 1:4 ratio. Water was added to a beaker with a magnetic stirring rod until a vortex was able to form.

each additional layer of target material must have an appreciable contribution to the total number of reactions occurring. For any target, based on Eq. 5.15, reaction rate vs. spherical radius follows a decreasing exponential curve. To ensure each addition of target material contributes an appreciable amount to the total number of reactions occurring, the target size is chosen to stay on the linear part of the curve. Due to the reaction rate dependence on the mean free path, the optimal target size will change depending on the target being used.

6.2 ^{102}Ru(n, α)^{99}Mo

An ^{102}Ru(n, α)^{99}Mo reaction is proposed for the production of ^{99}Mo. Natural ruthenium can be used as the target, in the form of ruthenium oxide (RuO_2) suspended in water. Ruthenium occurs naturally as 7 different isotopes shown in Table 6.1, with ^{102}Ru being the most abundant. During the irradiation, neutrons can interact with any of the nuclei within the target to produce a number of reaction products, which are shown in Fig. 6.2. Of all the reaction products, only 5 unique elements are present, which are Ru, Mo, Tc, Rh, and Pd. Each of these elements have the potential to be separated via recoil and to end up in the solution. Once the initial filtration of the solution and target grains has occurred, the solution can be chemically separated in order to produce a pure molybdenum product. Along with long lived Mo isotopes, there are two radioactive isotopes of molybdenum present; ^{101}Mo, and ^{99}Mo. ^{101}Mo has a half life of $\sim$15 minutes, which is very short relative to the 66 h half life of ^{99}Mo. This means the target can wait for 10 half lives or 150 minutes in

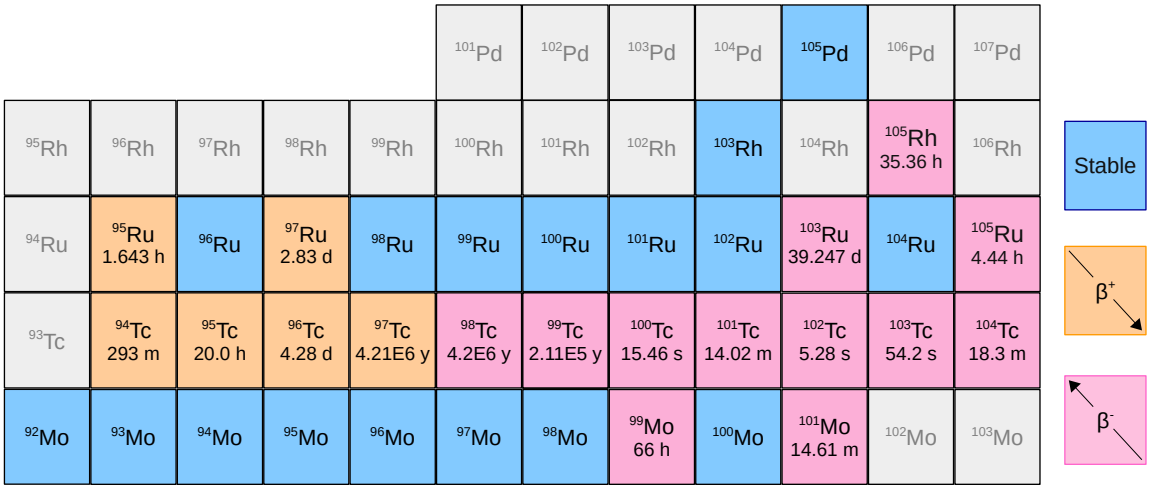

Figure 6.2: All possible products as a result of Ruthenium activation [15]. Blue indicates stable isotopes, orange indicates excited isotopes that undergo β^+ emission, and pink indicates excited isotopes that undergo β^- emission.

order for the ^{101}Mo to decay before the chemical separation, and the purification will result in a Mo product, with the only radioactive isotope being ^{99}Mo, the isotope of interest.

In order to predict the amount of ^{99}Mo produced, target parameters discussed in Chapter 5 are determined, starting with the isotopic density of ^{nat}Ru, ^{16}O, and H within the sample, along with their corresponding (n, total) cross sections. The results for all Ru isotopes are shown in Table 6.1, and the results for ^{16}O and H are shown in Table 6.2.

Table 6.1: Naturally occurring ruthenium isotopes and their abundances. Density of nuclei for each isotope is calculated according to Eq. 5.7, and (n, total) cross sections for 14.1 MeV neutrons given in units of barns were obtained from NNDC [15].

Isotope	**% Ab**	η_n **[1/cm^3]**	**(n, total) σ [b]**
96	5.54	1.75×10^{21}	4.53885
98	1.87	5.89×10^{20}	4.53796
99	12.76	4.02×10^{21}	4.5374
100	12.60	3.97×10^{21}	4.53705
101	17.06	5.66×10^{21}	4.03051
102	31.55	9.95×10^{21}	4.03375
104	18.62	5.87×10^{21}	4.0789

The mean free path of 7.92 cm was calculated for a target composed of $^{nat}RuO_2$ and H_2O, with a volume ratio $V_R = 0.2$, following Eq. 5.11 using isotopic abundances, densities, and cross sections from Table 6.1 and Table 6.2. Using this value to calculate the reaction rate, the ideal size of the target is chosen such that the reaction rate is still within the linear region and each increase in target size increases the number of reaction products by an appreciable amount. The reaction rate for a shell of thickness, dr, for increasing shell

Table 6.2: Volume density, molar mass, and the molecular density for ruthenium target components. Density of nuclei for each isotope is calculated following Eq. 5.7, and (n, total) cross sections for 14.1 MeV neutrons given in units of barns were obtained from NNDC [15].

Molecule	ρ $\left[\mathbf{g/cm^3}\right]$	**M** [g/mol]	η_m $\left[\mathbf{1/cm^3}\right]$	**Isotope**	η_n $\left[\mathbf{1/cm^3}\right]$	**(n, total)** σ **[b]**
RuO_2	6.97	133.098	$3.15\times\ 10^{22}$	^{nat}Ru	See table 6.1	See table 6.1
				^{16}O	$6.31\ \times\ 10^{22}$	1.5964
H_2O	1.0	18.02	3.34×10^{22}	^{1}H	$6.69\ \times10^{22}$	0.6852
				^{16}O	$3.34\ \times10^{22}$	1.5964

size is shown in Fig. 6.8. A radius of 2 cm has been chosen as it is well within the linear region, and will be used for production calculations.

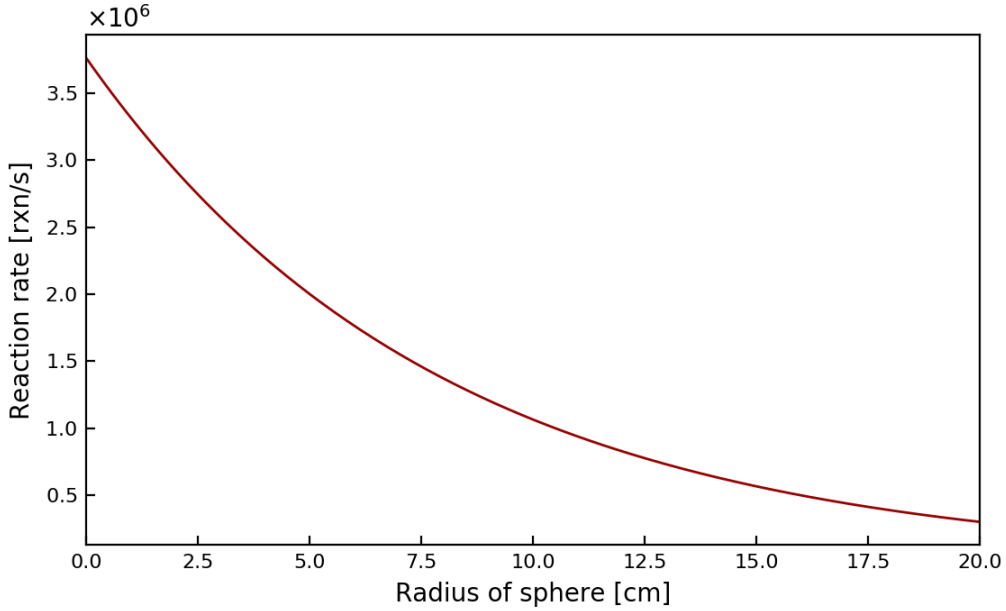

Figure 6.3: ^{nat}Ru reaction rates calculated as a function of spherical radius. Reaction rate is calculated for a spherical shell of 0.1 cm, at the radius, r, from the center.

The cross section for the reaction of interest, ^{102}Ru(n, α)^{99}Mo , is plotted as a function of incident neutron energy in Fig. 6.4. For the 14.1 MeV neutrons used in this study, the (n, α) cross section is determined to be 5.4551 mb [15]. The mean free path of the ^{102}Ru(n, α)^{99}Mo reaction given the volume ratio of 0.2 is calculated to be $9.21\ \times\ 10^4$ cm, and the branching ratio calculated according to Eq. 5.16 is $8.60\ \times\ 10^{-5}$. The activity of ^{99}Mo that can theoretically be produced is shown in Fig. 6.5 for 3 different neutron fluxes that are common in commercial neutron generators over 3 of the ^{99}Mo 66 h half lives [46]. The exempt quantity of $1\ \times\ 10^6$ Bq is also shown for reference, and indicates the amount of allowed activity that can be produced given the current NSL licensing [47].

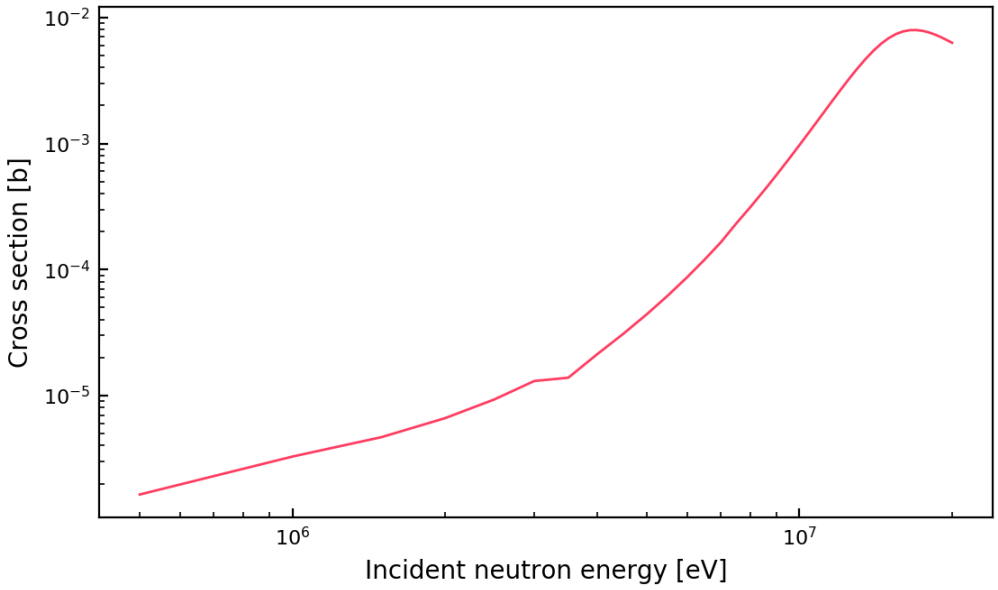

Figure 6.4: ^{102}Ru cross sections as a function of incident neutron energy for (n, α) reaction. The reaction cross section for 14.1 MeV energy neutrons is 0.0054551 b [15].

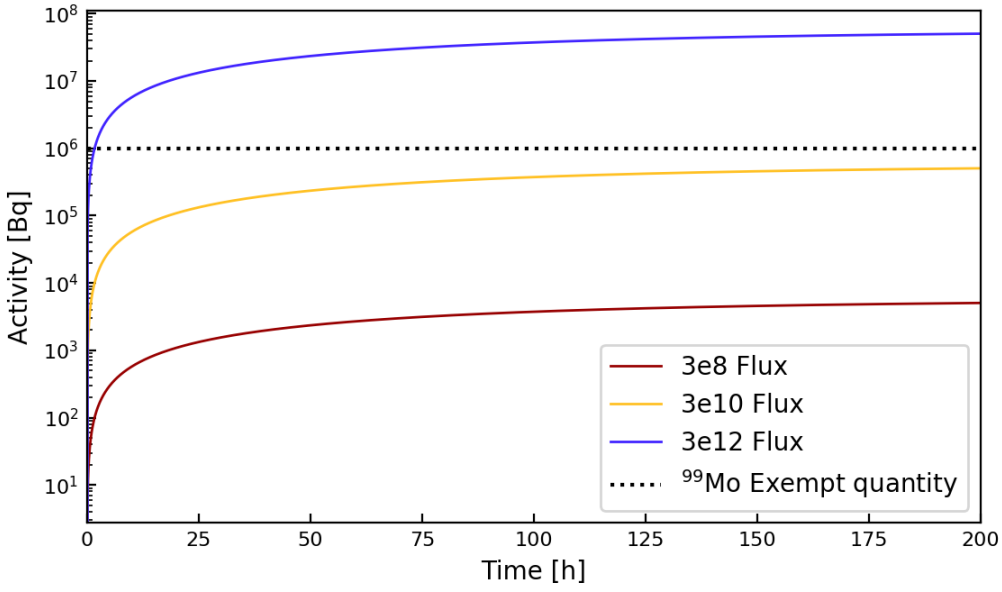

Figure 6.5: ^{99}Mo production is plotted as a function of irradiation length for a spherical target with a radius of 2 cm. Production is shown for 3 common fluxes; 3×10^8, 3×10^{10}, and 3×10^{12} neutrons/s. The exempt quantity is from the Government of Canada website [47].

These calculations for the ^{99}Mo production as a result of neutron irradiation shows that an appreciable amount of ^{99}Mo can theoretically be produced by the NSL. For preliminary experiments, a sample of Al will be used, instead of the Ru. This is first and foremost due to the comparitive cost and accessibility of Ru. Al provides a cheap, easily accessible alternative that can be used for target optimization experiments, and recoil separation experiments, as it undergoes an (n, α) reaction to produce ^{24}Na, a radioactive isotope of sodium.

Figure 6.6: All possible products as a result of aluminum activation. Blue indicates stable isotopes, orange indicates excited isotopes that undergo β^+ emission, and pink indicates excited isotopes that undergo β^- emission.

For preliminary experiments, an aluminum source has been chosen as a target component to undergo an (n, α) reaction to produce radioactive sodium-24 (^{24}Na) from aluminum-27 (^{27}Al). This is the same reaction mechanism used for the activation of ^{102}Ru to produce ^{99}Mo, making this a good analogue. Furthermore, the cost and accessibility of aluminum makes this an ideal testing ground to develop the isotope producer project. The grains and solvent that make up the target that will be used for preliminary experiments are alumina (Al_2O_3) and water, respectively. Al is isotopically pure, with 100% of natural aluminum being the ^{27}Al isotope. All possible products of any 14.1 MeV neutron reaction on ^{27}Al are shown in Fig. 6.6. Elements in the final product are Al, Mg, Na, Ne, Si, and F, with only Al, Na, and Mg having radioactive species existing past a few minutes. The only radioactive Na present is the isotope of interest, ^{24}Na, so secondary separation can occur immediately following irradiation.

In order to predict the amount of ^{24}Na produced during irradiation, target parameters discussed in Chapter 5 are determined, starting with the isotopic density of ^{27}Al, ^{16}O, and H within the sample, along with their corresponding (n, total) cross sections. Results are shown in Table 6.3.

Table 6.3: Volume density, molar mass, and the molecular density for aluminum target components. Density of nuclei for each isotope is calculated following Eq. 5.7, and (n, total) cross sections for 14.1 MeV neutrons given in units of barns were obtained from NNDC [15].

Molecule	ρ $\left[\mathbf{g/cm^3}\right]$	**M** $\mathbf{[g/mol]}$	η_m $\left[\mathbf{1/cm^3}\right]$	**Isotope**	η_n $\left[\mathbf{1/cm^3}\right]$	**(n, total)** σ **[b]**
Al_2O_3	3.965	101.96	$2.34\times\ 10^{22}$	^{27}Al	$4.68\times\ 10^{22}$	1.7443
				$^{16}O_s$	$7.03\ \times\ 10^{22}$	1.5964
H_2O	1.0	18.02	3.34×10^{22}	^{1}H	$6.69\ \times\ 10^{22}$	0.6852
				$^{16}O_l$	$3.34\ \times\ 10^{22}$	1.5964

Following Eq. 5.11 and data from Table 6.3, the mean free path of 8.47 cm was calculated for a target composed of $^{27}Al_2O_3$ and H_2O, with a volume ratio $X_V = 0.2$. Using this value to calculate the reaction rate, the ideal size of the target is chosen such that the reaction rate is still within the linear region and each increase in the targets spherical radius increases the number of reaction products by an appreciable amount. The reaction rate for a shell of thickness, dr, for increasing shell size is shown in Fig. 6.8. A radius of 2 cm has been chosen for consistency with the ^{99}Mo study and because it is within the linear region.

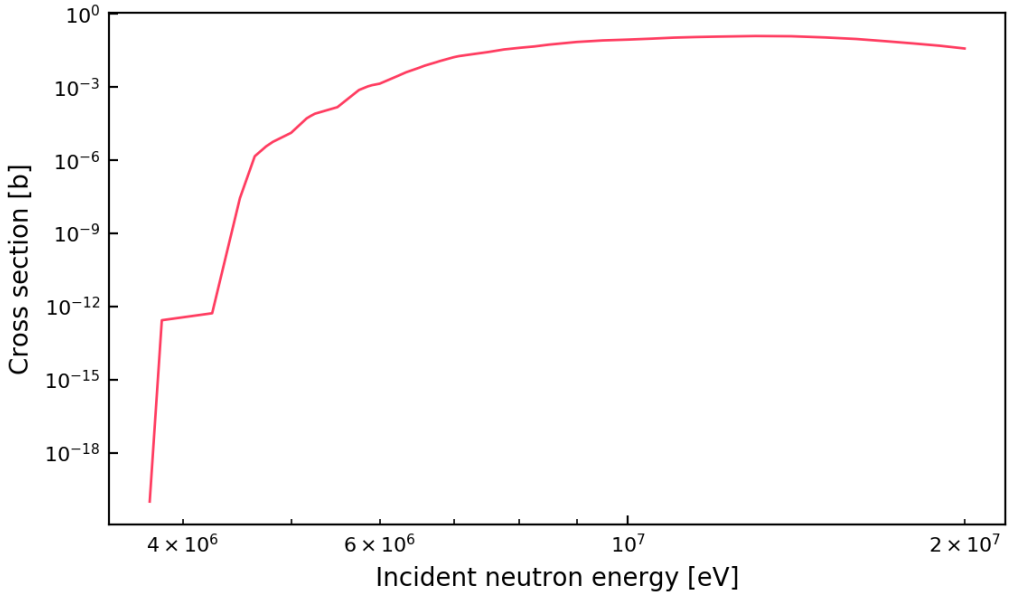

Figure 6.7: ^{27}Al cross sections as a function of incident neutron energy for (n, α) reaction. The reaction cross section for 14.1 MeV energy neutrons is 0.122509 b [15].

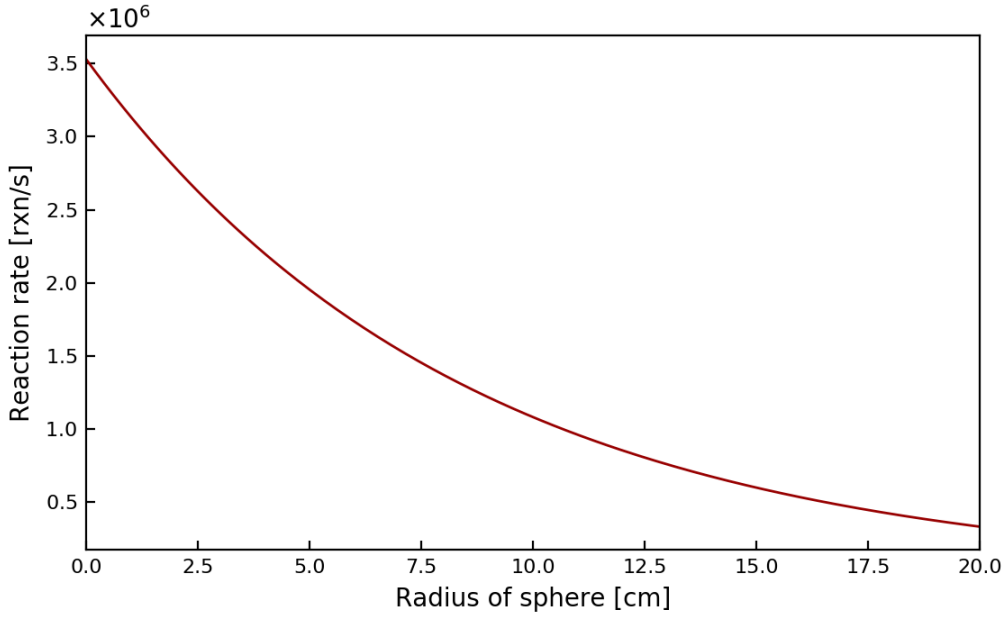

Figure 6.8: ^{27}Al reaction rates calculated as a function of spherical radius. Reaction rate is calculated for a spherical shell of 0.1 cm, at the radius, r, from the center.

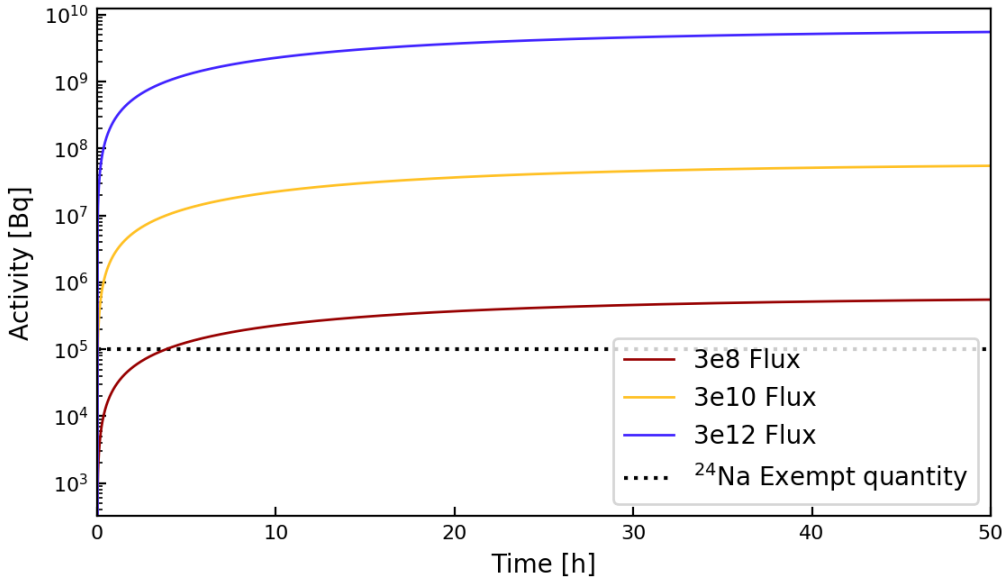

Figure 6.9: ^{24}Na production is plotted as a function of irradiation length for a spherical target with a radius of 2 cm. Production is shown for 3 common fluxes; 3×10^8, 3×10^{10}, and 3×10^{12} neutrons/s. The exempt quantity is 10^5 as reported on the Government of Canada website [47].

The cross section for the reaction of interest, ^{27}Al(n, α)^{24}Na , is plotted as a function of incident neutron energy in Figure 6.7. For the 14.1 MeV neutrons used in this study, the (n, α) cross section is found to be 0.122509 b [15]. The mean free path of the ^{27}Al(n, α)^{24}Na reaction given the volume ratio of 0.2 is calculated to be 8.71 $\times$ 10^2 cm, and the branching ratio calculated according to Eq. 5.16 is 9.70 $\times$ 10^{-3}. The activity of ^{24}Na that can theoretically be produced is shown in Fig. 6.9 for 3 different neutron fluxes that are common in commercial neutron generators over 3 ^{24}Na half lives [46]. The exempt quantity of 1 $\times$ 10^5 Bq is also shown for reference, and indicates the amount of allowed activity that can be produced given the current NSL licensing [47].

6.4 ^{27}Al(n, α)^{24}Na Results

In order to determine of the amount of separation that has occurred due to recoil from the (n, α) reaction, a sample was made consisting of 7.372 g of alumina powder with nominal particle size of $\sim$ 45 μm - 250 μm mixed with 12.786 g of water. Prior to the irradiation, the sample was shaken to make a homogeneous mixture, and then placed next to the NG accelerator tube, unperturbed during the irradiation. The sample was irradiated for $\sim$1 h at maximum neutron flux, and then transferred to a centrifuge that was run for $\sim$10 m at $\sim$3300 rpm. The solution was decanted into a syringe fitted with a glass wool filter, and transferred to a second vial that will henceforth be referred to as Sample A. The remaining target was left in the original vial, and will henceforth be referred to as Sample B. The vials were weighed before and after being filled, with weights reported in Table 6.4. Sample A contained 7.4796 g of the solution, Sample B had a remaining 12.5683 g of the original target, and there was a 0.0466 g loss of product which occurred during filtration through the syringe. Sample A was transferred to the GEARS detector for a $\sim$24 hour measurement, followed by Sample B for a $\sim$93 h measurement. The timeline of the sample starting at the beginning of irradiation and ending with the end of the measurement of Sample B is shown in Fig. 6.10.

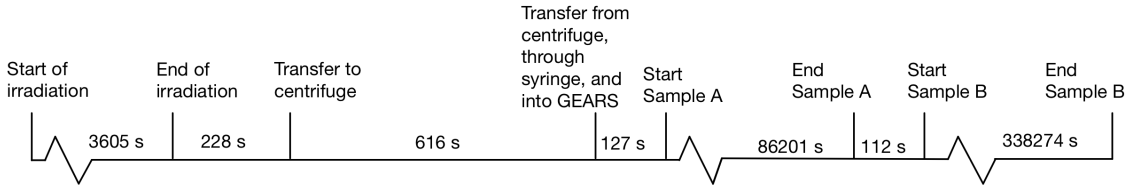

Figure 6.10: Timeline of ^{27}Al activation experiment. The experiment begins at the start of the neutron irradiation of the sample. The time was marked when the irradiation was completed, when the sample was placed into the centrifuge, and when the sample was removed from the centrifuge. Once the sample was split into two separate samples, A and B, the time was marked when both samples were placed in the detector, and removed from the detector.

Table 6.4: Masses of the vials and target components for all three samples during the experiment. The analytical balance used has a standard deviation of 0.0002 g.

Object	**Mass (g)**
Irradiated Vial	6.6655
Aluminum Oxide	7.3720
Water	12.7860
Total Mass of Irradiated Vial	26.8172
Vial for separated solution	6.6636
Separated solution	7.4796
Remaining product in irradiated vial	12.5683
Syringe and glass filter	7.9979
Syringe and filter after separation	8.0245
Product lost in syringe	0.0466

Spectra taken using the GEARS detector for Sample A and Sample B are shown in Fig. 6.11, and Fig. 6.12, respectively. As expected, both spectra show prominent peaks at characteristic ^{24}Na energies of 1368 and 2754 keV. Peaks for ^{27}Mg energies of 844 and 1014 keV are present in the spectrum for Sample A, but not for Sample B. This is because the half life of ^{27}Mg is only 9.38 m, and any ^{27}Mg present in Sample B had long since decayed prior to the measurement. Spectra shown in Fig. 6.11 and 6.12 show that the activation of Al was successful in producing the ^{24}Na isotope.

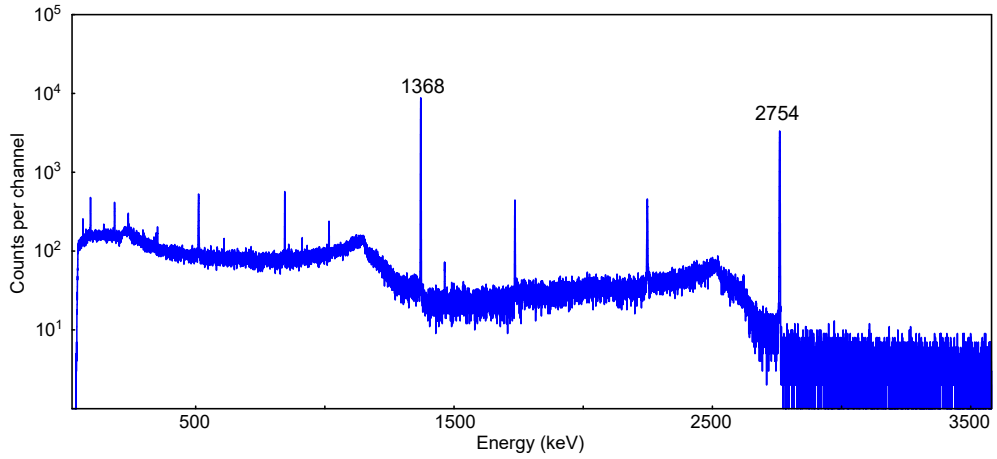

Figure 6.11: The measured γ-ray spectrum for solution separated from the target following irradiation and centrifugation is shown. The solution was measured for ∼24 h. Characteristic ^{24}Na peaks at 1368 keV and 2754 keV are visible, indicating the presence of ^{24}Na in the solution.

A separation factor is determined by doing time resolved energy peak analysis for the 1368 keV γ-ray transistion in both samples, following the procedure outlined in Sec. 3.3. Time resolved peak fitting is shown in Fig. 6.13 and Fig. 6.14 for Sample A and B, respectively. The number of ^{24}Na nuclei in each sample at the beginning of their measurements

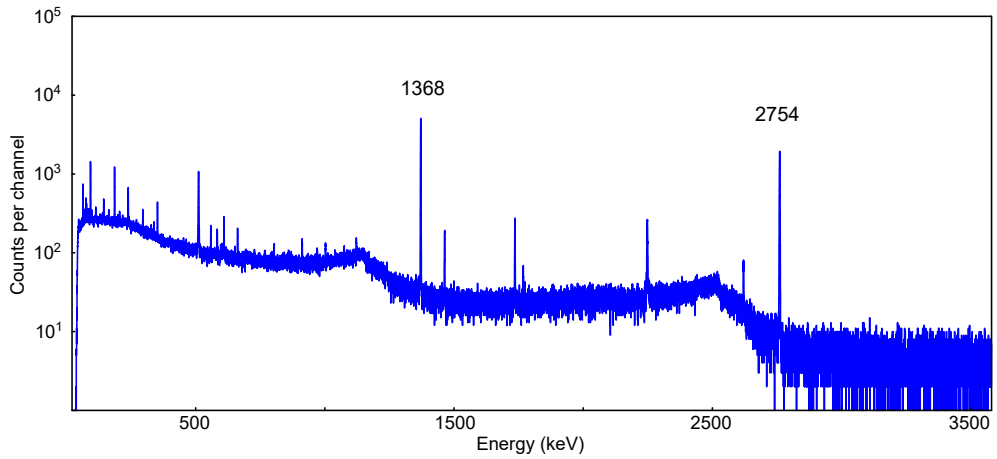

Figure 6.12: The measured γ-ray spectrum for the remaining target material following irradiation, centrifugation, and removal of solution. The remaining target material was measured for ∼93 h. Characteristic ^{24}Na peaks at 1368 keV and 2754 keV are visible, indicating the presence of ^{24}Na in the remaining target material.

was calculated to be 9.64(4) × 10^4 and 3.67(2) × 10^4 for Sample A and B, respectively. The corresponding activities are calculated according to Eq. 3.15 with the decay constant, λ equal to 1.28 × 10^{-5} 1/s, and detection efficiency for the γ-ray energy of 1368 keV equal to 0.00176(14)%. The activity of Sample A and B at the beginning of their respective measurements are 703(3) Bq and 268(1) Bq. The activity in the sample at the end of irradiation is determined following

$$A(t=0) = A(t_d)e^{\lambda t_d}, \tag{6.1}$$

where t_d is the time between the creation of the samples, and the start of the measurement. Sample A and B were created during the transfer of the original target from the centrifuge, through the syringe, and into the vial. This was taken to be 60 s before the measurement of Sample A was begun, and 86373 s before the measurement of Sample B was begun. At the time of creation, the activity of Sample A was 704(3) Bq, Sample B was 812(4) Bq, and the total activity was 1516(5) Bq. Results are shown in Table 6.5. It is important to note that although the detector was calibrated prior to measurements as detailed in Section 3.2, the calibration was completed using point sources positioned 10.5 cm above the GEARS detector can. The geometric factor was not calculated for the sample vials used to hold Samples A and B, and thus the results for the activity of the samples is not exact. However, the geometry of Samples A and B are identical so the relative activity is not affected.

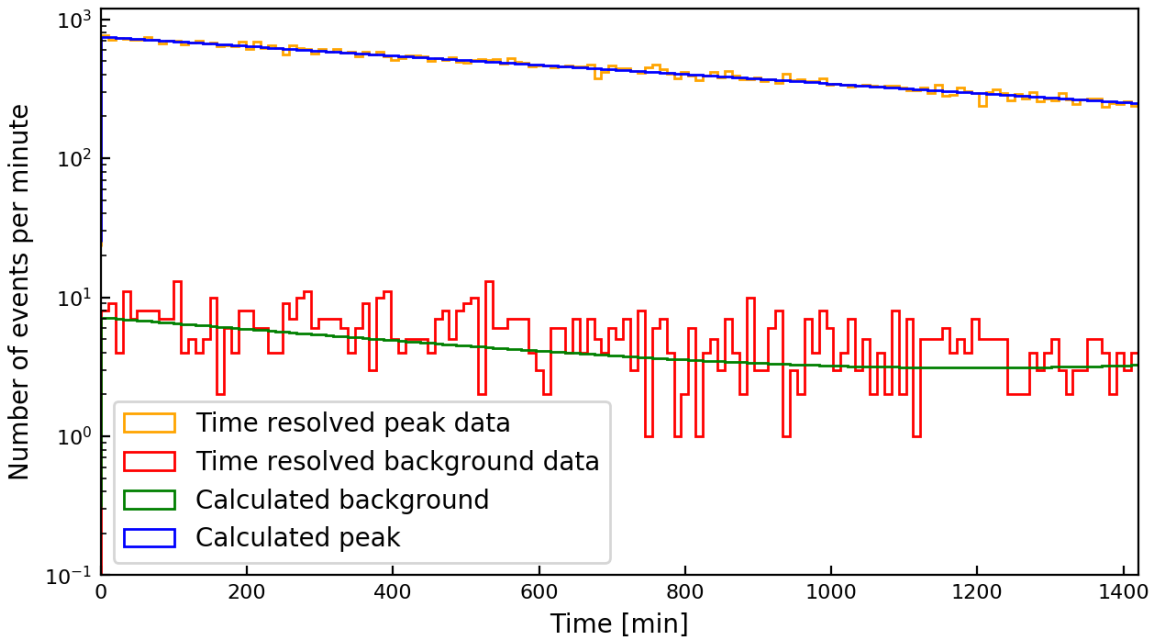

Figure 6.13: The time resolved spectrum of 1368 keV peak of Sample A is shown in orange. The best fit curve established using the minimum χ^2 estimation for determining best fit parameters is shown in blue, with a reduced $\chi^2_\nu = 1.01$. The background data is shown in red, while the calculated background is shown in green.

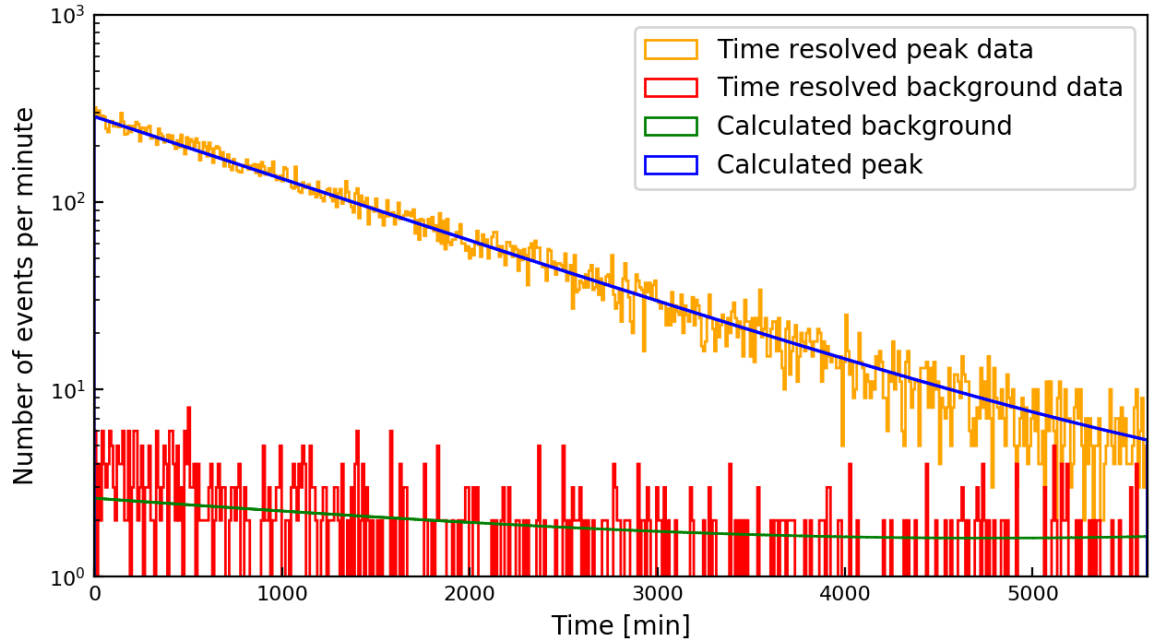

Figure 6.14: The time resolved spectrum of 1368 keV peak of Sample B is shown in orange. The best fit curve established using the minimum χ^2 estimation for determining best fit parameters is shown in blue, with a reduced $\chi^2_\nu = 1.19$. The background data is shown in red, while the calculated background is shown in green.

Table 6.5: Summary of results of Al activation experiment, including the number of ^{24}Na nuclei detected in Sample A and Sample B, and the activity of both when they were separated from one another.

Sample	$\mathbf{N_0}$	$\mathbf{t_d}$ **[s]**	$\mathbf{A(t_d)}$ **[Bq]**	$\mathbf{A(t_c)}$ **[Bq]**
A	$9.64(4) \times 10^4$	60	703(3)	704(3)
B	$3.67(2) \times 10^4$	86373	268(1)	812(4)

The separation factor is calculated following

$$\text{Separation Factor} = \frac{A_A(t_c)}{A_A(t_c) + A_B(t_c)} \cdot 100\%, \tag{6.2}$$

A_A and A_B are the activities of Samples A and B respectively, and t_c is the time the samples were created. The separation factor was calculated to be 46.4(4)%.

6.5 Conclusion

In conclusion, a significant amount of ^{99}Mo can be produced via neutron activation of a ^{nat}Ru source, and the production of ^{24}Na via ^{27}Al(n, α)^{24}Na was successful. Furthermore, nuclear recoil is an effective method of separating reaction products from the bulk sample. This study is a successful proof of concept for the development of the isotope producer, and indicates that neutron activation is a viable method for production of radioisotopes. Continuing this study, the separation of the products from the bulk sample, possibility of scaling up production, and NSL capabilities for continuing this endeavor need to be addressed.

Chapter 7

Discussion

The isotope producer project is a promising method of isotope production, and with some development can help the NSL significantly broaden its experimental program. The experiments undertaken in this thesis have resulted in starting points for future projects to further develop the isotope producer project into a viable solution for the isotope crisis.

7.1 Generating simulations

The calculations completed to determine the viability of the isotope producer project were based on a very basic geometry. Although this is sufficient for a proof of concept, having a more detailed simulation can take into account the actual geometry of the neutron generator, as well as easily simulate the irradiation for different lengths of time, target compositions, and target geometries. Modelling would be done using the Geometry and Tracking version 4 (Geant4) framework in order to accurately determine the amount of activity produced during irradiation based on the placement of the target in relation to the neutron generator, the target size, shape, and target container parameters, and determine how those factors impact the production during irradiation [48, 49]. This type of modelling can also be used when scaling up, in order to optimize the placement of the sample in relation to multiple neutron generators to achieve maximum production.

7.2 Separation

The separation achieved was ∼46% of the total activity produced, done via centrifugation and filtration of the products through a syringe packed with glass wool. This separation is proof that the nuclear recoil of the products out of the target grains is an effective way to separate the product from reactants, and is expected given the neutron energy and the α emission. Szilard and Chalmers were able to achieve ∼50% separation using themal neutrons to induce (n, γ) reactions. Although the preliminary ^{27}Al(n, α)^{24}Na experiment was not optimized in any way, the high energy of the neutrons and the increased recoil energy resulting from the emission of an α particle compared to a γ-ray can explain the

separation achieved. To further investigate the separation by recoil process, a simulation can be created, and additional experiments can be undertaken.

In order to increase the separation due to recoil, further studies on the target composition will first be carried out. From the preliminary studies it is not evident what is causing the retention of the reaction products within the target grains. Possibilities are that the reaction products do not have enough energy to recoil out of the grains, or the reaction products are sticking to the sides of the grain. Proposed studies to address the aformentioned possibilities are to vary the size of the grains, and to try using a different solvent [50, 51, 52, 53]. Finally the filtration of the solvent from the grains will need to be investigated further. Currently, filtration is accomplished using a centrifuge and decanting the solvent through a syringe. Although a large portion of the solvent is removed there is still an appreciable amount remaining with the grains that contributes to a loss of product and potentially a lower separation ratio. Ideally, the majority of the separation process will be completed during recoil.

Once the recoil separation and filtration has been investigated and optimized, the purification of the products can be implemented. In order to have a useful product, the isotope has to have a high specfic activity and be isotopically pure. As previously discussed the elemental isotopic purity can be achieved by the recoil separation and waiting appropriate times for contaminants to decay. The remaining contaminants in the solvent will need to be chemically separated, and the remaining product can be concentrated to achieve ideal specific activity. Purification studies have not begun and are one of the next steps that need to be taken for the completion of the isotope producer project.

7.3 Product transfer

The transfer of reaction products from the irradiation position and NG vault to the detector can take upwards of 3 minutes. For isotopes with long half lives such as ^{24}Na or ^{99}Mo, this is not a problem, but for shorter lived isotopes with $t_{1/2}$ on the order of minutes, transfer time can be an appreciable amount of the isotopes lifetime, and a faster transfer is critical for accurate analysis of the sample. In addition, the use of radioisotopes requires minimal interference or exposure to the workers in order to minimize the dose acquired. In order to decrease transfer time and minimize exposure of workers, a pneumatic tube is in place to connect the vault to the lab. One of the next planned developments of the NSL is to implement the pneumatic tube so that samples can be automatically transferred from the vault and into the lab following irradiation. Having this system in place will streamline and remove human uncertainty from the transferring process. Additionally automatic transfer can help with the accuracy of measurements as the time it takes for the transfer can be determined more accurately than for the self-timed Student Running As Fast As Possible (SRAFAP) method which is currently employed.

7.4 Experimental analysis

All analysis has been done using the GEARS detector. This method is sufficient, but does pose problems for shorter lived isotopes, isotopes with gamma energies in the low energy ranges, and with small amounts of activity. Due to the passive shielding, there is huge contamination from Compton scattering in the low energy regions. As well, the geometry of the detector restricts the sample size and placement in relation to the detector, resulting in samples being placed very closed to the detection can, increasing background at low energy ranges. Another issue encountered during the analysis of the samples is that the separation of the product resulted in two separate samples to be analyzed. This becomes a problem for isotopes with short half lives, as the second sample needs to be analyzed before it decays while the first sample would need to be analyzed long enough to obtain sufficient counting statistics. To this end, the addition of a secondary detection system would greatly benefit the analysis of this study. This would make the analysis more efficient, and allow for longer detection times and higher detected number of counts, and more accurate results due to the higher counting statistics.

Another aspect of the analysis that would require attention in order to advance the development of the isotope producer is geometric simulations of the target within the detector. For the experimental determination of the separation ratio discussed in Sec. 6.4, Samples A and B both had the same volume and geometry, and thus no geometric considerations had to be taken into account for the detection efficiency. However, if the volume or geometry of the samples under comparison were to be different, the detection efficiency would have to be determined for each individual sample geometry. Additionally, if two separate detection systems were used as proposed, the efficiency of the samples in each detector would need to be individually determined as well. Fortunately, this has been done in the past for evironmental studies carried out by the NSL, and the Geant4 framework can be used [54].

7.5 Scaling up production

Neutron induced activation as a method for production of radioisotopes is advantageous due to the scaling capabilities. A neutron generator costs ~$200000, which is much cheaper than alternatives such as the cost of a nuclear reactor or cyclotron infrastructure [55]. Although the amount of activity produced in the preliminary experiment was low, Fig. 6.5 and Fig. 6.9 show that an appreciable amount of activity can be produced, given a long enough irradiation time. However, increasing the length gives diminishing returns and beyond a certain point, does not result in increased production. For a larger product yield, the number of neutrons and/or the number of reactants needs to be increased, as seen in Eq. 5.12. Due to the size restrictions imposed by the mean free path, seen in the calculations of reaction rate as a funtion of spherical radius, the size of the target can not be increased infinitely to increase production. However, increasing the neutron flux and thus the number

of neutrons, the reaction rate can be increased, which would increase the number of products as seen in Figures 6.9 and 6.5. For reference, a typical ^{99m}Tc generator is made with 2 Ci or 74 GBq of ^{99}Mo [56]. This amount was not reached in the calculations with the highest flux, and the amount of possible produced activity is approaching the order of 10^8 Bq. Although this amount is unattainable using the specified 2 cm radius sphere and NG with flux of 10^{12} n/s/cm^2, by adjusting the parameters as discussed it is well within reach, indicating that fast neutron induced isotope production of ^{99}Mo is viable.

7.6 Conclusion

The ground work for the development of an isotope producer at the NSL has been completed with preliminary experiments for the determination of the amount of activity that can be produced for ^{99}Mo , and ^{24}Na . Additionally, it was shown that the Szilard-Chalmers reaction is an effective method of recoil separation of reaction products, with a separation ratio of 46.4(4)% achieved following the irradiation of ^{27}Al to produce ^{24}Na. These promising results are motivation to continue work on refining the recoil separation by adjusting target parameters, and developing a simulation for the irradiation to accurately predict the reaction rates for different target compositions and geometries. Although the quantities required for commercial production are far beyond the capabilities of the NSL, quantities required for scientific research is attainable. By developing the infrastructure for an isotope producer, the NSL can engage in collaborations with research groups requiring specific isotopes and contribute to a wide variety of research projects.

Bibliography

[1] A. Vertes, S. Nagy, Z. Klencsar, and R. G. Lovas, *Handbook of nuclear chemistry*, pp. 143–385. Dordrecht ; Heidelberg: Springer, 2nd ed., 2011.

[2] K. S. Krane and D. Halliday, *Introductory nuclear physics*, pp. 160–431. New York: Wiley, 1987.

[3] G. F. Knoll, *Radiation detection and measurement*, pp. 307–426. New York: Wiley, 3rd ed., 2000.

[4] K. Siegbahn, ed., *Alpha-, beta- and gamma-ray spectroscopy*, pp. 1–76. Amsterdam [u.a.] New York: North-Holland Publ. Comp, 5th ed., 1979.

[5] N. Tsoulfanidis and S. Landsberger, *Measurement and detection of radiation*, pp. 217–230. 2015.

[6] "GEM P-type Coaxial High Purity Germanium (HPGe) Radiation Detectors | AMETEK ORTEC." `https://www.ortec-online.com/products/radiation-detectors/germanium-hpge-radiation-detectors/hpge-radiation-detector-types-how-choose/gem-p-type-coaxial-hpge-radiation-detectors`.

[7] T. A. Domingo, *Time-resolved gamma-ray spectroscopy with the GEARS detector: Applications in environmental radionuclide monitoring and neutron activation analysis*. Thesis, Science: Department of Chemistry, Aug. 2017.

[8] A. S. Chester, *Monitoring rainwater and seaweed reveals the presence of ^{131}I in southwest and central British Columbia, Canada following the Fukushima nuclear accident in Japan*. Thesis, Science: Department of Chemistry, Aug. 2013.

[9] SFU NUSC, "LN2 filling procedure." `http://www.sfu.ca/~nusc/fillLN2.html`, July 2020.

[10] "Midas Wiki." `https://midas.triumf.ca/MidasWiki/index.php/`, July 2020.

[11] SFU NUSC, "Tipsort." `https://github.com/SFUNUSC/TIPsort`, July 2020.

[12] D. C. Radford, "gf3." `https://radware.phy.ornl.gov/gf3/gf3.html`, June 2020.

[13] D. C. Radford, "Plot, pedit, and plot2ps documentation." `https://radware.phy.ornl.gov/plot.html`, June 2020.

[14] G. A. F. Seber and A. J. Lee, *Linear regression analysis*, pp. 97–137. Wiley series in probability and statistics, Hoboken, N.J: Wiley-Interscience, 2nd ed., 2003.

[15] "National Nuclear Data Center." `https://www.nndc.bnl.gov/`, June 2020.

[16] I. Hughes and T. P. A. Hase, *Measurements and their uncertainties: a practical guide to modern error analysis*, pp. 23–83. Oxford: New York : Oxford University Press, 2010.

[17] *Nuclear Technology Review 2010*, pp. 50–55. Non-serial Publications, Vienna: International Atomic Energy Agency.

[18] P. W. Atkins and J. De Paula, *Physical chemistry*, pp. 622–652. New York: W.H. Freeman, 9th ed., 2010.

[19] H. Naik, S. V. Suryanarayana, K. C. Jagadeesan, S. V. Thakare, P. V. Joshi, V. T. Nimje, K. C. Mittal, A. Goswami, V. Venugopal, and S. Kailas, "An alternative route for the preparation of the medical isotope ^{99}Mo from the ^{238}U(γ, f) and ^{100}Mo(γ, n) reactions," *Journal of Radioanalytical and Nuclear Chemistry*, vol. 295, pp. 807–816, Jan. 2013.

[20] N. R. C. (U.S.), ed., *Medical isotope production without highly enriched uranium*, pp. 7–89. Washington, D.C: National Academies Press, 2009.

[21] *Technetium-99m radiopharmaceuticals: manufacture of kits*. No. 466 in Technical reports series / International Atomic Energy Agency, Vienna: Internat. Atomic Energy Agency, 2008.

[22] R. Boyd, "Technetium-99m generators - The available options," *The International Journal of Applied Radiation and Isotopes*, vol. 33, pp. 801–809, Oct. 1982.

[23] D. Hamilton and P. J. Riley, *Diagnostic nuclear medicine: a physics perspective*, pp. 26–29. Berlin ; New York: Springer, 2004.

[24] S. Bastawrous, P. Bhargava, F. Behnia, D. S. W. Djang, and D. R. Haseley, "Newer PET Application with an Old Tracer: Role of ^{18}F-NaF Skeletal PET/CT in Oncologic Practice," *RadioGraphics*, vol. 34, pp. 1295–1316, Sept. 2014.

[25] R. A. Pagnanelli and D. A. Basso, "Myocardial Perfusion Imaging with ^{201}Tl," *Journal of Nuclear Medicine Technology*, vol. 38, pp. 1–3, Mar. 2010.

[26] A. A. Ghotbi, A. Kjaer, and P. Hasbak, "Review: comparison of PET rubidium-82 with conventional SPECT myocardial perfusion imaging," *Clinical Physiology and Functional Imaging*, vol. 34, pp. 163–170, May 2014.

[27] OECD and Nuclear Energy Agency, *The supply of medical isotopes an economic diagnosis and possible solutions*, pp. 78–111. 2019.

[28] R. Van Noorden, "Radioisotopes: The medical testing crisis," *Nature*, vol. 504, pp. 202–204, Dec. 2013.

[29] T. Ruth, "Accelerating production of medical isotopes," *Nature*, vol. 457, pp. 536–537, Jan. 2009.

[30] P. Gould, "Medical isotope shortage reaches crisis level," *Nature*, vol. 460, pp. 312–313, July 2009.

[31] E. Broussard, IAEA Office of Public Information and Communication, "Medical Radioisotopes still Produced but Facing Distribution Challenges Globally, Data Collected by IAEA Shows." https://www.iaea.org/newscenter/news/medical-radioisotopes-still-produced-but-facing-distribution-challenges-globally-data-collected-by-iaea-shows, June 2020.

[32] "Air transport improves for medical radioisotopes : Covid-19 - World Nuclear News." https://world-nuclear-news.org/Articles/Air-transport-bottleneck-easing-for-medical-radioi, June 2021.

[33] S. C. van der Marck, A. J. Koning, and K. E. Charlton, "The options for the future production of the medical isotope ^{99}Mo," *European Journal of Nuclear Medicine and Molecular Imaging*, vol. 37, pp. 1817–1820, Oct. 2010.

[34] P. Schaffer, K. Gagnon, T. J. Morley, D. Abrams, M. S. Kovacs, S. A. McQuarrie, S. K. Zeisler, F. Benard, and T. J. Ruth, "Direct on-target production of 99mTc using the 100Mo(p,2n)99mTc transformation," *Nuclear Medicine and Biology*, vol. 37, pp. 713–714, Aug. 2010.

[35] B. Guerin, S. Tremblay, S. Rodrigue, J. A. Rousseau, V. Dumulon-Perreault, R. Lecomte, J. E. van Lier, A. Zyuzin, and E. J. van Lier, "Cyclotron production of 99mtc: an approach to the medical isotope crisis," *Journal of Nuclear Medicine*, vol. 51, pp. 13N–16N, Apr. 2010.

[36] "P 385 Neutron Generator." http://www.thermofisher.com/order/catalog/product/10135952.

[37] J. Williams, A. Chester, T. Domingo, U. Rizwan, K. Starosta, and P. Voss, "Neutron generator facility at SFU: Geant4 dose rate predication and verification," *Radiation Protection Dosimetry*, vol. 171, no. 3, pp. 313–325, 2016.

[38] K. Almenas and R. Lee, *Nuclear Engineering*, pp. 53–82. Berlin, Heidelberg: Springer Berlin Heidelberg, 1992.

[39] M.-A. Menezes, *Advances in neutron activation analysis of large objects with emphasis on archaeological examples: Results of a coordinated research project*, pp. 5–17. Vienna: International Atomic Energy Agency, 2018.

[40] "Neutron Activation Analysis | The McClellan Nuclear Research Center." https://mnrc.ucdavis.edu/neutron-activation-analysis, May 2020.

[41] G. R. Choppin, J.-O. Liljenzin, and J. Rydberg, "Production of Radionuclides," in *Radiochemistry and Nuclear Chemistry*, pp. 388–414, Elsevier, 2002.

[42] L. Szilard and T. A. Chalmers, "Detection of Neutrons Liberated from Beryllium by Gamma Rays: a New Technique for Inducing Radioactivity," *Nature*, vol. 134, pp. 494–495, Sept. 1934.

[43] L. Szilard and T. A. Chalmers, "Chemical Separation of the Radioactive Element from its Bombarded Isotope in the Fermi Effect," *Nature*, vol. 134, pp. 462–462, Sept. 1934.

[44] G. Harbottle and N. Sutin, "The Szilard-Chalmers Reaction in Solids," in *Advances in Inorganic Chemistry and Radiochemistry*, vol. 1, pp. 267–314, Elsevier, 1959.

[45] City of Burnaby, "City of Burnaby: Annual Drinking Water Quality Report 2019."

[46] K.-N. Leung, J. K. Leung, and G. Melville, "Feasibility study on medical isotope production using a compact neutron generator," *Applied Radiation and Isotopes*, vol. 137, pp. 23–27, July 2018.

[47] L. S. Branch, "Consolidated federal laws of canada, Nuclear Substances and Radiation Devices Regulations." `https://laws.justice.gc.ca/eng/regulations/sor-2000-207/page-8.html`, June 2020.

[48] S. Agostinelli, J. Allison, K. Amako, J. Apostolakis, H. Araujo, P. Arce, M. Asai, D. Axen, S. Banerjee, G. Barrand, F. Behner, L. Bellagamba, J. Boudreau, L. Broglia, A. Brunengo, H. Burkhardt, S. Chauvie, J. Chuma, R. Chytracek, G. Cooperman, G. Cosmo, P. Degtyarenko, A. Dell'Acqua, G. Depaola, D. Dietrich, R. Enami, A. Feliciello, C. Ferguson, H. Fesefeldt, G. Folger, F. Foppiano, A. Forti, S. Garelli, S. Giani, R. Giannitrapani, D. Gibin, J. J. GÃşmez Cadenas, I. GonzÃąlez, G. Gracia Abril, G. Greeniaus, W. Greiner, V. Grichine, A. Grossheim, S. Guatelli, P. Gumplinger, R. Hamatsu, K. Hashimoto, H. Hasui, A. Heikkinen, A. Howard, V. Ivanchenko, A. Johnson, F. W. Jones, J. Kallenbach, N. Kanaya, M. Kawabata, Y. Kawabata, M. Kawaguti, S. Kelner, P. Kent, A. Kimura, T. Kodama, R. Kokoulin, M. Kossov, H. Kurashige, E. Lamanna, T. LampÃľn, V. Lara, V. Lefebure, F. Lei, M. Liendl, W. Lockman, F. Longo, S. Magni, M. Maire, E. Medernach, K. Minamimoto, P. Mora de Freitas, Y. Morita, K. Murakami, M. Nagamatu, R. Nartallo, P. Nieminen, T. Nishimura, K. Ohtsubo, M. Okamura, S. O'Neale, Y. Oohata, K. Paech, J. Perl, A. Pfeiffer, M. G. Pia, F. Ranjard, A. Rybin, S. Sadilov, E. Di Salvo, G. Santin, T. Sasaki, N. Savvas, Y. Sawada, S. Scherer, S. Sei, V. Sirotenko, D. Smith, N. Starkov, H. Stoecker, J. Sulkimo, M. Takahata, S. Tanaka, E. Tcherniaev, E. Safai Tehrani, M. Tropeano, P. Truscott, H. Uno, L. Urban, P. Urban, M. Verderi, A. Walkden, W. Wander, H. Weber, J. P. Wellisch, T. Wenaus, D. C. Williams, D. Wright, T. Yamada, H. Yoshida, and D. Zschiesche, "Geant4 – a simulation toolkit," *Nuclear Instruments and Methods in Physics Research Section A: Accelerators, Spectrometers, Detectors and Associated Equipment*, vol. 506, pp. 250–303, July 2003.

[49] J. Allison, K. Amako, J. Apostolakis, H. Araujo, P. Arce Dubois, M. Asai, G. Barrand, R. Capra, S. Chauvie, R. Chytracek, G. Cirrone, G. Cooperman, G. Cosmo, G. Cuttone, G. Daquino, M. Donszelmann, M. Dressel, G. Folger, F. Foppiano, J. Generowicz, V. Grichine, S. Guatelli, P. Gumplinger, A. Heikkinen, I. Hrivnacova, A. Howard, S. Incerti, V. Ivanchenko, T. Johnson, F. Jones, T. Koi, R. Kokoulin, M. Kossov, H. Kurashige, V. Lara, S. Larsson, F. Lei, O. Link, F. Longo, M. Maire, A. Mantero, B. Mascialino, I. McLaren, P. Mendez Lorenzo, K. Minamimoto, K. Murakami, P. Nieminen, L. Pandola, S. Parlati, L. Peralta, J. Perl, A. Pfeiffer, M. Pia, A. Ribon, P. Rodrigues, G. Russo, S. Sadilov, G. Santin, T. Sasaki, D. Smith, N. Starkov, S. Tanaka, E. Tcherniaev, B. Tome, A. Trindade, P. Truscott, L. Urban, M. Verderi, A. Walkden, J. Wellisch, D. Williams, D. Wright, and H. Yoshida,

"Geant4 developments and applications," *Institute of Electrical and Electronics Engineers Transactions on Nuclear Science*, vol. 53, pp. 270–278, Feb. 2006. Conference Name: IEEE Transactions on Nuclear Science.

[50] G. Harbottle, "Szilard-Chalmers Reaction in Crystalline Compounds of Chromium," *The Journal of Chemical Physics*, vol. 22, pp. 1083–1088, June 1954.

[51] G. R. Choppin, J.-O. Liljenzin, J. Rydberg, and C. Ekberg, *Radiochemistry and nuclear chemistry*, pp. 388–414. Amsterdam ; Boston: Elsevier/AP, Academic Press is an imprint of Elsevier, 4th ed., 2013.

[52] J. Jach and G. Harbottle, "Reactions of recoil bromine atoms in alkali bromates," *Transactions of the Faraday Society*, vol. 54, pp. 520–525, 1958.

[53] R. Galea and K. Moore, "Production of a carrier-free standard ^{56}Mn source for the NRC manganese salt bath," *Applied Radiation and Isotopes*, vol. 154.108896, Dec. 2019.

[54] T. Domingo, K. Starosta, A. Chester, J. Williams, S. J. Lehnert, N. Gantner, and J. J. Alava, "Fukushima-derived radioactivity measurements in Pacific salmon and soil samples collected in British Columbia, Canada," *Canadian Journal of Chemistry*, vol. 96, pp. 124–131, Feb. 2018.

[55] P. Schmor, "Review of Cyclotrons for the Production of Radioactive Isotopes for Medical and Industrial Applications," *Reviews of Accelerator Science and Technology*, vol. 04, pp. 103–116, Jan. 2011. Publisher: World Scientific Publishing Co.

[56] "Human Health Campus - ^{99}Mo to ^{99m}Tc radionuclide principles." `https://humanhealth.iaea.org/HHW/Radiopharmacy/VirRad/Eluting_the_Generator/Generator_Module/99Mo_-_99mTc_radionuclide_principles/index.html`, July 2020.

[57] D. J. Griffiths, *Introduction to quantum mechanics*, pp. 435–455. Upper Saddle River, NJ: Pearson Prentice Hall, 2nd ed., 2005.

[58] N. N. D. Center, "Q-value Calculator (QCalc) Results." `https://www.nndc.bnl.gov/qcalc/qcalcr.jsp`, May 2020.

Appendix A

Least Squares Analysis

Least squares fitting is a method used to find the best set of parameters for a function, f. This method utilizes χ^2 defined as

$$\chi^2 = \sum_i \frac{1}{\omega_i^2}(y_i - f(x_i))^2 \tag{A.1}$$

where y_i is the measurement, $f(x_i)$ is the function that depends on the parameters and relates x_i to y_i, and ω_i the standard error in y_i. The best fit parameters of the function, f are found by minimizing χ^2 with respect to the parameters. A fit is considered successful when the best fit parameters are found such that

$$\chi^2_{min} \approx d.o.f = D - p \tag{A.2}$$

where χ^2_{min} is the minimized χ^2 calculated following Eq. A.1 with the best fit parameters, $d.o.f$ is the number of degrees of freedom, D is the number of data points, and p is the number of free parameters.

All least squares fitting referenced in this thesis is completed analytically using a linearized χ^2 specific to the problem and is described on a case by case basis [57].

Appendix B

First order χ^2 fitting

To find the best fit parameters for a linear equation, the χ^2 function takes the form

$$\chi^2 = \sum_{i=0}^{N} \frac{(y_i - a_0 - a_1 x_i)^2}{\omega_i^2}. \tag{B.1}$$

The first derivative of the χ^2 function is taken with respect to the coefficients to give

$$\frac{\partial \chi^2}{\partial a_0} = 0 = \sum_{i=0}^{N} \frac{y_i}{\omega_i^2} - a_0 \sum_{i=0}^{N} \frac{1}{\omega_i^2} - a_1 \sum_{i=0}^{N} \frac{x_i}{\omega_i^2} \tag{B.2}$$

$$\frac{\partial \chi^2}{\partial a_1} = 0 = \sum_{i=0}^{N} \frac{y_i x_i}{\omega_i^2} - a_0 \sum_{i=0}^{N} \frac{x_i}{\omega_i^2} - a_1 \sum_{i=0}^{N} \frac{x_i^2}{\omega_i^2}. \tag{B.3}$$

The coefficients can be solved for using matrix algebra in which Eq. B.2 and Eq. B.3 are rewritten as

$$\begin{bmatrix} \sum_{i=0}^{N} \frac{1}{\omega_i^2} & \sum_{i=0}^{N} \frac{x_i}{\omega_i^2} \\ \sum_{i=0}^{N} \frac{x_i}{\omega_i^2} & \sum_{i=0}^{N} \frac{x_i^2}{\omega_i^2} \end{bmatrix} \quad \begin{bmatrix} a_0 \\ a_1 \end{bmatrix} \quad = \quad \begin{bmatrix} \sum_{i=0}^{N} \frac{y_i}{\omega_i^2} \\ \sum_{i=0}^{N} \frac{y_i x_i}{\omega_i^2} \end{bmatrix}. \tag{B.4}$$

Following Cramer's Rules, a_0 and a_1 are given by

$$a_0 = \frac{\sum \frac{y_i}{\omega_i^2} \sum \frac{x_i^2}{\omega_i^2} - \sum \frac{x_i}{\omega_i^2} \sum \frac{y_i x_i}{\omega_i^2}}{\sum \frac{1}{\omega_i^2} \sum \frac{x_i^2}{\omega_i^2} - \sum \frac{x_i}{\omega_i^2} \sum \frac{x_i}{\omega_i^2}} \tag{B.5}$$

$$a_1 = \frac{\sum \frac{1}{\omega_i^2} \sum \frac{y_i x_i}{\omega_i^2} - \sum \frac{y_i}{\omega_i^2} \sum \frac{x_i}{\omega_i^2}}{\sum \frac{1}{\omega_i^2} \sum \frac{x_i^2}{\omega_i^2} - \sum \frac{x_i}{\omega_i^2} \sum \frac{x_i}{\omega_i^2}} \tag{B.6}$$

Appendix C

Time resolved peak fitting

To find the best fit parameters for the time resolved peak fitting analysis, the χ^2 function takes the form

$$\chi^2 = \sum_{i=0}^{N} \frac{(\mathscr{P}_i - P_i)^2}{\omega_{\mathscr{P}_i}^2} + \sum_{i=0}^{N} \frac{(\mathscr{B}_i - B_i)^2}{\omega_{\mathscr{B}_i}^2} \tag{C.1}$$

where $\mathscr{P}_i$ is the data in the peak region of the spectrum, $\mathscr{B}_i$ is the data in the background region of the spectrum, N is the number of data points, and $\omega_{\mathscr{P}_i}$ and $\omega_{\mathscr{B}_i}$ are the uncertainty in counts of $\mathscr{P}_i$ and $\mathscr{B}_i$, respectively. γ-ray counting experiments follow Poissonian statistics, which allows for the following substitutions,

$$\begin{aligned} \omega_{\mathscr{P}_i} &= \sqrt{\mathscr{P}_i} \\ \omega_{\mathscr{B}_i} &= \sqrt{\mathscr{B}_i}. \end{aligned} \tag{C.2}$$

For clarity, P_i given by Eq. 3.14 and B_i given by Eq. 3.13 are rewritten as

$$\Sigma_i = P_0 n_i + b_0 \mathscr{b}_{0i} + b_1 \mathscr{b}_{1i} + b_2 \mathscr{b}_{2i} \tag{C.3}$$

$$B_i = b_0 \mathscr{b}_{0i} + b_1 \mathscr{b}_{1i} + b_2 \mathscr{b}_{2i} \tag{C.4}$$

where

$$
\begin{aligned}
n_i &= e^{-\lambda t_i}(1 - e^{-\lambda \Delta t}) \\
\mathcal{b}_{0i} &= \Delta t \\
\mathcal{b}_{1i} &= \frac{\Delta t^2}{2} + \Delta t t_i \\
\mathcal{b}_{2i} &= \frac{\Delta t^3}{3} + \Delta t^2 t_i + \Delta t t_i^2
\end{aligned}
\tag{C.5}
$$

The χ^2 is minimized with respect to the parameters, N_0, b_0, b_1, and b_2 by taking the first derivative of the χ^2 function with respect to each parameter to give

$$
\frac{\partial \chi^2}{\partial N_0} = 0 = \sum_{i=0}^{N} \frac{1}{\omega_{\mathscr{P}_i}^2} \left[-\mathscr{P}_i n_i + N_0 n_i^2 + b_0 \mathcal{b}_{0i} n_i + b_1 \mathcal{b}_{1i} n_i + b_2 \mathcal{b}_{2i} n_i \right] \tag{C.6}
$$

$$
\begin{aligned}
\frac{\partial \chi^2}{\partial b_0} = 0 = &\sum_{i=0}^{N} \frac{1}{\omega_{\mathscr{P}_i}^2} \left[-\mathscr{P}_i \mathcal{b}_{0i} + N_0 n_i \mathcal{b}_{0i} + b_0 \mathcal{b}_{0i}^2 + b_1 \mathcal{b}_{1i} \mathcal{b}_{0i} + b_2 \mathcal{b}_{2i} \mathcal{b}_{0i} \right] \\
&+ \sum_{i=0}^{N} \frac{1}{\omega_{\mathscr{B}_i}^2} \left[-\mathscr{B}_i \mathcal{b}_{0i} + b_0 \mathcal{b}_{0i}^2 + b_1 \mathcal{b}_{1i} \mathcal{b}_{0i} + b_2 \mathcal{b}_{2i} \mathcal{b}_{0i} \right]
\end{aligned}
\tag{C.7}
$$

$$
\begin{aligned}
\frac{\partial \chi^2}{\partial b_1} = 0 = &\sum_{i=0}^{N} \frac{1}{\omega_{\mathscr{P}_i}^2} \left[-\mathscr{P}_i \mathcal{b}_{1i} + N_0 n_i \mathcal{b}_{1i} + b_0 \mathcal{b}_{0i} \mathcal{b}_{1i} + b_1 \mathcal{b}_{1i}^2 + b_2 \mathcal{b}_{2i} \mathcal{b}_{1i} \right] \\
&+ \sum_{i=0}^{N} \frac{1}{\omega_{\mathscr{B}_i}^2} \left[-\mathscr{B}_i \mathcal{b}_{1i} + b_0 \mathcal{b}_{0i} \mathcal{b}_{1i} + b_1 \mathcal{b}_{1i}^2 + b_2 \mathcal{b}_{2i} \mathcal{b}_{1i} \right]
\end{aligned}
\tag{C.8}
$$

$$
\begin{aligned}
\frac{\partial \chi^2}{\partial b_2} = 0 = &\sum_{i=0}^{N} \frac{1}{\omega_{\mathscr{P}_i}^2} \left[-\mathscr{P}_i \mathcal{b}_{2i} + N_0 n_i \mathcal{b}_{2i} + b_0 \mathcal{b}_{0i} \mathcal{b}_{2i} + b_1 \mathcal{b}_{1i} \mathcal{b}_{2i} + b_2 \mathcal{b}_{2i}^2 \right] \\
&+ \sum_{i=0}^{N} \frac{1}{\omega_{\mathscr{B}_i}^2} \left[-\mathscr{B}_i \mathcal{b}_{2i} + b_0 \mathcal{b}_{0i} \mathcal{b}_{2i} + b_1 \mathcal{b}_{1i} \mathcal{b}_{2i} + b_2 \mathcal{b}_{2i}^2 \right]
\end{aligned}
\tag{C.9}
$$

which can be rewritten in matrix notation as

$$\begin{bmatrix} \sum \frac{1}{\omega^2_{\mathscr{P}_i}} n_i^2 & \sum \frac{1}{\omega^2_{\mathscr{P}_i}} n\mathcal{b}_{0i} & \sum \frac{1}{\omega^2_{\mathscr{P}_i}} n\mathcal{b}_{1i} & \sum \frac{1}{\omega^2_{\mathscr{P}_i}} n\mathcal{b}_{2i} \\ \sum \frac{1}{\omega^2_{\mathscr{P}_i}} n\mathcal{b}_{0i} & \sum \frac{1}{\omega^2_{\mathscr{P}_i}} \mathcal{b}_{0i}^2 + \sum \frac{1}{\omega^2_{\mathscr{B}_i}} \mathcal{b}_{0i}^2 & \sum \frac{1}{\omega^2_{\mathscr{P}_i}} \mathcal{b}_{1i}\mathcal{b}_{0i} + \sum \frac{1}{\omega^2_{\mathscr{B}_i}} \mathcal{b}_{1i}\mathcal{b}_{0i} & \sum \frac{1}{\omega^2_{\mathscr{P}_i}} \mathcal{b}_{2i}\mathcal{b}_{0i} + \sum \frac{1}{\omega^2_{\mathscr{B}_i}} \mathcal{b}_{2i}\mathcal{b}_{0i} \\ \sum \frac{1}{\omega^2_{\mathscr{P}_i}} n_i\mathcal{b}_{1i} & \sum \frac{1}{\omega^2_{\mathscr{P}_i}} \mathcal{b}_{0i}\mathcal{b}_{1i} + \sum \frac{1}{\omega^2_{\mathscr{B}_i}} \mathcal{b}_{0i}\mathcal{b}_{1i} & \sum \frac{1}{\omega^2_{\mathscr{P}_i}} \mathcal{b}_{1i}^2 + \sum \frac{1}{\omega^2_{\mathscr{B}_i}} \mathcal{b}_{1i}^2 & \sum \frac{1}{\omega^2_{\mathscr{P}_i}} \mathcal{b}_{2i}\mathcal{b}_{1i} + \sum \frac{1}{\omega^2_{\mathscr{B}_i}} \mathcal{b}_{2i}\mathcal{b}_{1i} \\ \sum \frac{1}{\omega^2_{\mathscr{P}_i}} n_i\mathcal{b}_{2i} & \sum \frac{1}{\omega^2_{\mathscr{P}_i}} \mathcal{b}_{0i}\mathcal{b}_{2i} + \sum \frac{1}{\omega^2_{\mathscr{B}_i}} \mathcal{b}_{0i}\mathcal{b}_{2i} & \sum \frac{1}{\omega^2_{\mathscr{P}_i}} \mathcal{b}_{1i}\mathcal{b}_{2i} + \sum \frac{1}{\omega^2_{\mathscr{B}_i}} \mathcal{b}_{1i}\mathcal{b}_{2i} & \sum \frac{1}{\omega^2_{\mathscr{P}_i}} \mathcal{b}_{2i}^2 + \sum \frac{1}{\omega^2_{\mathscr{B}_i}} \mathcal{b}_{2i}^2 \end{bmatrix} \begin{bmatrix} N_0 \\ b_0 \\ b_1 \\ b_2 \end{bmatrix}$$

$$= \begin{bmatrix} \sum \frac{1}{\omega^2_{\mathscr{P}_i}} \mathscr{P}_i n_i \\ \sum \frac{1}{\omega^2_{\mathscr{P}_i}} \mathscr{P}_i \mathcal{b}_{0i} + \sum \frac{1}{\omega^2_{\mathscr{B}_i}} \mathscr{B}_i \mathcal{b}_{0i} \\ \sum \frac{1}{\omega^2_{\mathscr{P}_i}} \mathscr{P}_i \mathcal{b}_{1i} + \sum \frac{1}{\omega^2_{\mathscr{B}_i}} \mathscr{B}_i \mathcal{b}_{1i} \\ \sum \frac{1}{\omega^2_{\mathscr{P}_i}} \mathscr{P}_i \mathcal{b}_{2i} + \sum \frac{1}{\omega^2_{\mathscr{B}_i}} \mathscr{B}_i \mathcal{b}_{2i} \end{bmatrix} \tag{C.10}$$

or in short form,

$$\mathbf{M} \cdot \bar{a} = \bar{v}, \tag{C.11}$$

where M is the 4x4 matrix, $\bar{a}$ is the vector of parameters, and $\bar{v}$ is a vector of terms that are independent of free parameters for each of the expressions in Eq. C.6 - C.9. Following Cramer's rule, the solution for the parameters can be found by inverting the 4x4 matrix to yield

$$\bar{a} = \mathbf{M}^{-1} \cdot \bar{v}. \tag{C.12}$$

In order to find the error in the parameter N_0, it is convenient to expand Eq. C.1 to give

$$\chi^2 = \sum_{i=0}^{N} \frac{\mathscr{P}_i^2 + P_i^2 - 2\mathscr{P}_i P_i}{\omega^2_{\mathscr{P}_i}} + \sum_{i=0}^{N} \frac{\mathscr{B}_i^2 + B_i^2 - 2\mathscr{B}_i B_i}{\omega^2_{\mathscr{B}_i}} \tag{C.13}$$

and making the appropriate substitutions, rewrite it as

$$\chi^2 = C - 2\bar{v}\bar{a} + \bar{a}\mathbf{M}\bar{a}, \tag{C.14}$$

where C, is given by

$$C = \sum \mathscr{P}_i + \sum \mathscr{B}_i \tag{C.15}$$

and Eq. C.11 implies that

$$\bar{a}\mathbf{M}\bar{a} = \bar{v}\bar{a} = \bar{a}\bar{v}, \tag{C.16}$$

resulting in

$$\chi^2_{min} = C - \bar{v}\bar{a}. \tag{C.17}$$

The uncertainties in parameters are determined by establishing an error ellipse around the point by changing χ^2_{min} by $c_{p,\alpha}$, which depends on the number of parameters, p, and desired confidence level, α. The uncertainties in the parameters are constrained to the surface of the ellipse, and can be written in vector format similar to the parameters vector, $\bar{a}$, following

$$\bar{\delta_a} = [\delta_{N_0}, \delta_{b_0}, \delta_{b_1}, \delta_{b_2}]. \tag{C.18}$$

The uncertainty in the parameters can then be determined by writing Eq. C.14 as

$$\begin{aligned}
\chi^2(\bar{a} + \bar{\delta_a}) &= C - 2\bar{v}(\bar{a} + \bar{\delta_a}) + (\bar{a} + \bar{\delta_a})M(\bar{a} + \bar{\delta_a}) \\
\chi^2_{min} + c_{p,\alpha} &= C - 2\bar{v}\bar{a} - 2\bar{v}\bar{\delta_a} + \bar{a}M\bar{a} + \bar{\delta_a}M\bar{a} + \bar{a}M\bar{\delta_a} + \bar{\delta_a}M\bar{\delta_a} \\
&= C - 2\bar{v}\bar{a} - 2\bar{v}\bar{\delta_a} + \bar{v}\bar{a} + \bar{\delta_a}\bar{v} + \bar{v}\bar{\delta_a} + \bar{\delta_a}M\bar{\delta_a} \\
&= C - \bar{v}\bar{a} + \bar{\delta_a}M\bar{\delta_a} \\
&= \chi^2_{min} + \bar{\delta_a}M\bar{\delta_a} \\
c_{p,\alpha} &= \bar{\delta_a}M\bar{\delta_a}.
\end{aligned} \tag{C.19}$$

For the purposes of this thesis, the only uncertainty of interest is δ_{N_0}, as the uncertainties in the background parameters will not contribute to the uncertainty in the determination of the activity of the source. Before solving for the error in N_0, M is rewritten as

$$\mathbf{M} = \begin{bmatrix} M_{00} & \bar{\nu_b}^T \\ \bar{\nu_b} & m \end{bmatrix} \tag{C.20}$$

where M_{00} is the entry of $\mathbf{M}$ given by

$$M_{00} = \sum \frac{1}{\omega^2_{\mathscr{P}_i}} n_i^2, \tag{C.21}$$

m is a 3x3 submatrix of M, and $\bar{\nu_b}$ is the remaining top row entries of M. The vector of parameter errors is also split so that the error in N_0 will be written independently of the remaining parameters, which are written as the vector

$$\bar{\delta_b} = [\delta_{b_0}, \delta_{b_1}, \delta_{b_2}]. \tag{C.22}$$

An exact solution for δ_{N_0} can be found using the method of Lagrange multipliers, as detailed in Appendix D, with the function $f(\delta_{N_0})$ defined by

$$f(\delta_{N_0}) = \delta_{N_0}, \tag{C.23}$$

under the constraint defined by

$$g(\bar{\delta_a}) = \bar{\delta_a}\mathbf{M}\bar{\delta_a} - c_{p,\alpha}. \tag{C.24}$$

The error δ_{N_0} is independent of the error in the remaining parameters, resulting in

$$\frac{\partial \delta_{N_0}}{\partial \bar{\delta_b}} = 0, \tag{C.25}$$

and is subject to the condition defined by Eq. C.19. Expanding $g(\bar{\delta_a})$ in order to write it as $g(\bar{\delta_b})$, the full Lagrangian is written as

$$\mathscr{L}(\delta_{N_0}, \bar{\delta_b}, \lambda) = \delta_{N_0} - \lambda\left(M_{00}\delta_{N_0}^2 + 2\delta_{N_0}\bar{v_b}\bar{\delta_b} + \bar{\delta_b}m\bar{\delta_b}\right) + \lambda c_{p,\alpha}. \tag{C.26}$$

The Lagrangian is solved by minimizing with respect to $\bar{\delta_b}$, and the multiplier λ such that they satisfy the conditions imposed by Eq. D.2. This results in the following two equations,

$$\begin{aligned} \frac{\partial \mathscr{L}}{\partial \bar{\delta_b}} &= 0 = -\lambda\left(2\delta_{N_0}\bar{v_b} + 2m\bar{\delta_b}\right) \\ \frac{\partial \mathscr{L}}{\partial \lambda} &= 0 = -M_{00}\delta_{N_0}^2 - 2\delta_{N_0}\bar{v_b}\bar{\delta_b} - \bar{\delta_b}m\bar{\delta_b} + c_{p,\alpha}, \end{aligned} \tag{C.27}$$

which can be rearranged to show

$$\begin{aligned} \bar{\delta_b} &= -\delta_{N_0}m^{-1}\bar{v_b} \\ c_{p,\alpha} &= M_{00}\delta_{N_0}^2 + 2\delta_{N_0}^2\bar{v_b}m^{-1}\bar{v_b} + \delta_{N_0}^2\bar{v_b}m^{-1}\bar{v_b}. \end{aligned} \tag{C.28}$$

The solution to this set of equations results in the error ε_{N_0} for the parameter N_0, given by

$$\varepsilon_{N_0} = \pm\sqrt{\frac{c_{p,\alpha}}{M_{00} + \bar{v_b}m^{-1}\bar{v_b}}}. \tag{C.29}$$

Appendix D

Lagrange Multipliers

The method of Lagrange multipliers is used as a strategy to find the local minima or maxima of a function that is constrained by one or more conditions. The general form of the Lagrangian in one dimension is given by

$$\mathscr{L}(x, \lambda) = f(x) - \lambda g(x), \tag{D.1}$$

where $f(x)$ is the function, $g(x)$ is the constraining condition, and λ is the Lagrange undetermined multiplier. The local maximum or minimum is found by constraining a point such that there exists λ_0 where (x_0, λ_0) is a stationary point, and the first partial derivatives of the Lagrangian are zero as seen in Eq. D.2.

$$\begin{aligned} \frac{\partial \mathscr{L}}{\partial x}|_{x_0\lambda_0} &= 0 \\ \frac{\partial \mathscr{L}}{\partial \lambda}|_{x_0\lambda_0} &= 0 \end{aligned} \tag{D.2}$$

Following Eq. D.2, there remains 2 equations and 2 unknowns that can be solved for.

Appendix E

Scaling data using χ^2 fit

Scaling data using the minimization of χ^2 is performed following the relation

$$\chi^2 = \sum_{i=1}^{N} \frac{(y_i - a_0 x_i)^2}{\sigma_i^2}. \tag{E.1}$$

To solve for the scaling factor, a_0, the first derivative of χ^2 is taken with respect to a_0 to give

$$\frac{\partial \chi^2}{\partial a_0} = 0 = -2 \sum_{i=1}^{N} \frac{x_i (y_i - a_0 x_i)}{\sigma_i^2}. \tag{E.2}$$

Eq. E.2 can then be rearranged to solve for a_0, yielding

$$a_0 = \frac{\sum_{i=1}^{N} \sigma_i^{-2} y_i x_i}{\sum_{i=1}^{N} \sigma_i^{-2} x_i^2} \tag{E.3}$$

Appendix F

α recoil

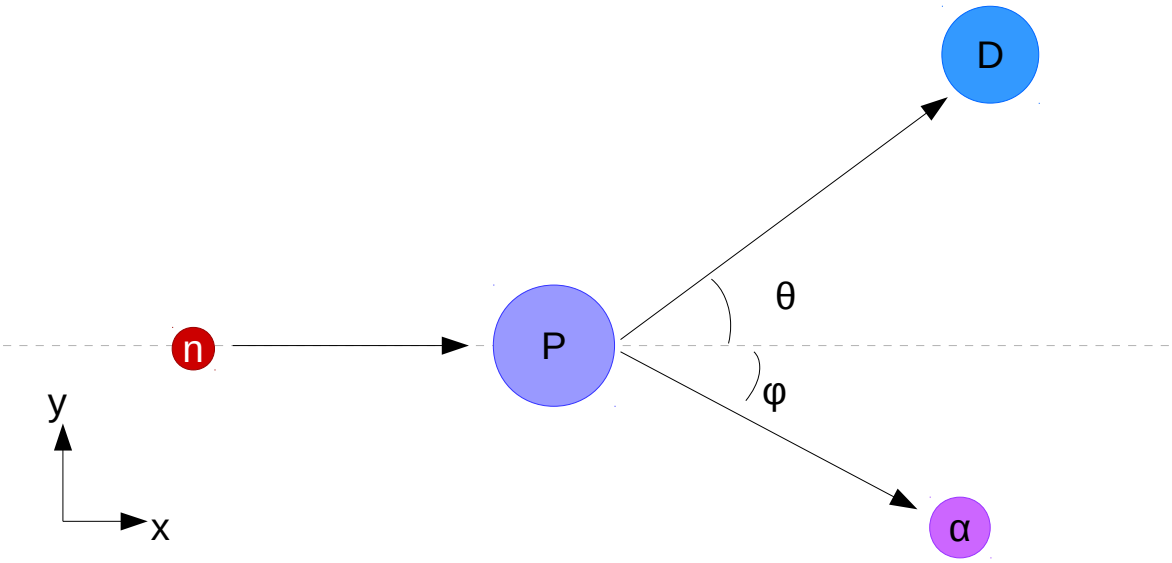

Figure F.1: Depiction of an $P(n,\alpha)D$ reaction occurring, with the α and D particles being ejected at angles ϕ and θ from the neutron's original trajectory, respectively.

In an $P(n,\alpha)D$ reaction, the neutron is the projectile moving towards the target nucleus, P, which is stationary. The resulting nucleus breaks into two particles; D and α. This reaction is shown in Fig. F.1. The energy of the recoiling α particle can be derived from the conservation of energy and momentum of the system. Conservation of momentum gives

$$\begin{aligned} p_n + p_P &= p_D \cos\theta + p_\alpha \cos\phi \\ 0 &= p_D \sin\theta + p_\alpha \sin\phi \end{aligned} \tag{F.1}$$

where p_n, p_P, p_D, and p_α are the momentum of the neutron, P, D, and the α particle. The first line of Eq. F.1 conserves the momentum along the horizontal axis, and the second line conserves momentum along the vertical axis. Conservation of energy gives

$$E_P + E_n = E_D + E_\alpha, \tag{F.2}$$

where E_P, E_n, E_D, and E_α are the energies of P, n, D, and α, respectively. The energy of a particle is made up of its kinetic and mass energy, and in the non-relativistic limit of $v \ll c$ where v is the velocity of a nuclei and c is the speed of light, can be written as

$$E \approx mc^2 + \frac{p^2}{2m} \tag{F.3}$$

where p is momentum, and m is the nuclear mass. In order to determine the energy of the resulting particle D and the emitted α, first the momentum of the α particle can be determined for the emission angle of $\theta = 0$ to π. Eq. F.1 can be rewritten following

$$\begin{aligned} p_\alpha^2 \cos^2\phi &= (p_n - p_D \cos\theta)^2 \\ p_\alpha^2 \sin^2\phi &= p_D^2 \sin^2\theta \\ p_\alpha^2 &= p_n^2 + p_D^2 - 2p_n p_D \cos\theta, \end{aligned} \tag{F.4}$$

and Eq. F.2 can be rewritten under the assumption that the target nuclei is at rest, using the nonrelativistic energy of a particle following

$$\begin{aligned} &m_n c^2 + \frac{p_n^2}{2m_n} + m_P c^2 = m_D c^2 + \frac{p_D^2}{2m_D} + m_\alpha c^2 + \frac{p_\alpha^2}{2m_\alpha} \\ &\frac{p_n^2}{2m_n} + (m_n + m_P - m_D - m_\alpha)c^2 = \frac{p_D^2}{2m_D} + \frac{p_\alpha^2}{2m_\alpha} \\ &E_{tot} = \frac{p_D^2}{2m_D} + \frac{p_\alpha^2}{2m_\alpha} \\ &p_\alpha^2 = 2m_\alpha \left(E_{tot} - \frac{p_D^2}{2m_D} \right). \end{aligned} \tag{F.5}$$

Setting the result of Eq. F.4 equal to the result of Eq. F.5 gives a quadratic expression in p_D,

$$0 = \left(1 - \frac{m_\alpha}{m_D}\right) p_D^2 - 2p_n \cos\theta p_D + p_n^2 - E_{tot} 2m_\alpha. \tag{F.6}$$

An expression for p_D dependent on the angle of emission, θ can be solved for using the quadratic formula to give

$$p_D = \frac{-p_n \cos\theta + \sqrt{p_n^2 \cos^2\theta - (1 - \frac{m_\alpha}{m_D})(p_n^2 - E_{tot} 2m_\alpha)}}{1 - \frac{m_\alpha}{m_D}}. \tag{F.7}$$

The corresponding momentum of the α particle dependent on θ is found following the result of Eq. F.4. The corresponding angle of emission, ϕ, of the α particle can then be found by rearranging the equation for conservation of momentum in the vertical axis as seen in Eq. F.1 to give

$$\phi = \sin^{-1}\left(\frac{p_D}{p_\alpha}\sin\theta\right). \tag{F.8}$$

Finally, the total kinetic energy, T, of D and α can be determined following

$$T = \frac{p^2}{2m}. \tag{F.9}$$

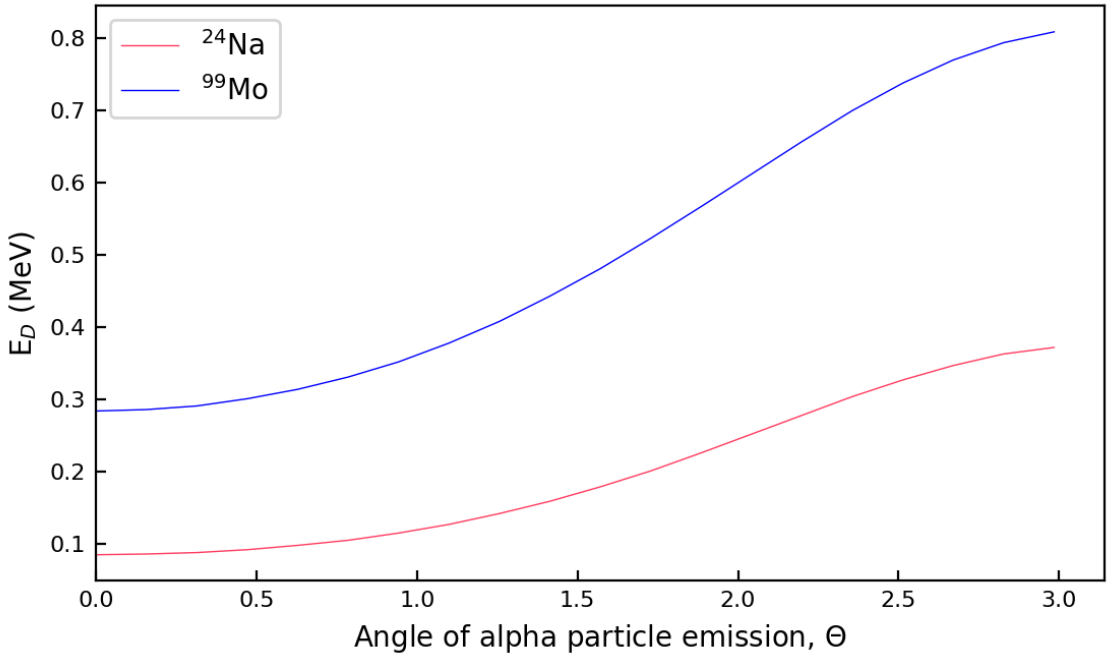

Figure F.2: The energy of D as a function of angle of emission of the α particle is shown for the ^{102}Ru(n, α)^{99}Mo reaction (blue) and the ^{27}Al(n, α)^{24}Na reaction (red).

The energies of the resulting particle D for the (n, α) reaction from ^{27}Al and ^{102}Ru are shown in Fig. F.2. For the ^{27}Al(n, α)^{24}Na reaction, ^{24}Na has kinetic energy, or recoil energy, ranging from 80 - 400 keV. For the ^{102}Ru(n, α)^{99}Mo reaction, ^{99}Mo has energy ranging from 280 - 820 keV. The reason the ^{102}Ru(n, α)^{99}Mo reaction results in a higher energy of the recoiling nucleus is because of the difference in rest mass energies of the nuclei taking part in the reaction. In Eq. F.5, a substitution is made for E_{tot} to give

$$E_{tot} = \frac{p_n^2}{2m_n} + Qc^2, \tag{F.10}$$

where Q is the difference in rest mass energy between the initial and final nuclei given by

$$Q = m_n + m_P - m_D - m_\alpha. \tag{F.11}$$

For both reactions, the kinetic energy of the neutron is equal to 14.1 MeV. The ^{27}Al(n, α)^{24}Na reaction has a Q value of -3.13 MeV, while the Q value for the ^{102}Ru(n, α)^{99}Mo reaction is 2.51 MeV [58].